

UNIVERSITY OF PADUA  
DEPARTMENT OF GEOSCIENCE  
MASTER'S DEGREE IN GEOPHYSICS FOR NATURAL  
RISKS AND RESOURCES

~ · ~

ACADEMIC YEAR 2024–2025

**Soil hydrology across scales: from  
soil moisture sensors to cosmic ray  
neutron sensing through  
geophysical characterization.**

**Supervisor**

Dott. Luca PERUZZO

**Co-Supervisor**

Prof. Giorgio CASSIANI

**Graduate Student**

Viola CIOFFI

2104282

FINAL EXAMINATION DATE: September 24, 2025

---



---

*A chi, nonostante tutto, vive ..  
a mia Madre, a mia Nonna, e ai miei Fratelli*



## **Abstract**

The quantification of subsurface moisture content is a complex topic of considerable importance in hydrogeophysics, with implications across a wide range of fields, from agriculture to natural hazard assessment. A cutting-edge technique that bridges the scales of remote sensing and local measurements is Cosmic Ray Neutron Sensing (CRNS), which is trivial in the data acquisition but highly complex and still in a developing phase, in terms of processing and interpretation. Following an introduction centred on neutron physics, this work presents an introductory study of CRNS applied to the lithological heterogeneities of a vineyard in Borgo Grignanello (Siena, Italy). The aim is to improve understanding of this emerging technique, with particular focus on key aspects of data processing, and to advance interpretation of measurements in heterogeneous sites. We combined a geophysical characterisation of the study area, using electrical resistivity tomography and electromagnetic induction, with analyses of soil samples and Monte Carlo simulations of neutron transport performed using URANOS, a software developed for environmental applications. In particular, we investigate the hypothesis that the behaviour of a heterogeneous system, under specific geometrical and hydrological conditions, can be approximated by that of a homogeneous site characterised by the properties of the drier region. The results support this hypothesis for the Borgo Grignanello site, demonstrating a clear affinity between the heterogeneous measurements and one of the two homogeneous models. This study highlights the potential of CRNS through an initial exploratory project, encouraging further research to refine the methodology and extend its application to real datasets

---

# Contents

<b>List of Figures</b>	<b>x</b>
<b>List of Tables</b>	<b>xii</b>
<b>Glossary</b>	<b>xiii</b>
<b>Introduction</b>	<b>1</b>
<b>1 Cosmic-ray neutrons</b>	<b>5</b>
1.1 The neutron . . . . .	5
1.1.1 Neutron Energies . . . . .	6
1.1.2 Neutron interactions . . . . .	6
1.2 Neutrons origin . . . . .	9
1.2.1 Primary cosmic-rays . . . . .	9
1.2.2 Secondary cosmic rays . . . . .	11
1.2.3 Neutron spectrum above the soil and modulation . . . . .	13
<b>2 Background on geophysical investigation methods</b>	<b>17</b>
2.1 Cosmic Ray Neutron Sensing . . . . .	17
2.1.1 Principles of the method . . . . .	17
2.1.2 Cosmic ray neutron detector . . . . .	19
2.1.3 Footprint and penetration depth . . . . .	21
2.2 Electrical resistivity tomography . . . . .	24
2.2.1 Principles . . . . .	25
2.3 Frequency domain electromagnetic induction method . . . . .	28
2.3.1 Principles . . . . .	29

<b>3</b>	<b>Material and Methods</b>	<b>33</b>
3.1	Study Site: Geology, Geomorphology and Vegetation . . . . .	33
3.2	Geophysical Data Acquisition and Processing . . . . .	36
3.2.1	Samples: Acquisition, Analysis, and Results . . . . .	37
3.2.2	ERT Survey: Acquisition, Processing, and Results . . . . .	42
3.2.3	FDEM Survey: Acquisition, Processing, and Results . . . . .	45
3.3	Modeling and Monte Carlo simulations . . . . .	49
3.3.1	URANOS Monte Carlo Transport Code . . . . .	49
3.3.2	Modeling Site conditions . . . . .	52
3.3.3	Footprint estimation . . . . .	53
3.3.4	Count - VWC curves . . . . .	55
3.3.5	Assessing the effect of the field heterogeneity . . . . .	57
<b>4</b>	<b>Results and Discussion</b>	<b>67</b>
4.1	Results from the Samples, ERT and EM . . . . .	67
4.2	Results from the simulations and analysis . . . . .	68
	<b>Conclusions</b>	<b>1</b>
	<b>Bibliography</b>	<b>8</b>

# List of Figures

1.1	Total cross section in barns for the interaction of neutrons with hydrogen (blue), oxygen (orange), silicon (green), and aluminum (red).	8
1.2	The effect of the Earth's magnetic field on cosmic-ray neutron intensity is shown by graphs of count rate as a function of geomagnetic vertical cutoff rigidity for a cosmic-ray neutron monitor (dots) [Goldhagen, 2003]. The curves are calculated [Clem and Dorman, 2000].	11
1.3	Global view of the primary cosmic ray spectrum obtained studying the produced cascades in the atmosphere with detectors on the ground that have large effective area for sampling such showers. [Gaisser, 2006]	12
1.4	Atmospheric depth dependencies of effective dose rates at $r_c = 0$ GV and solar minimum conditions [Weimar, 2022]	13
1.5	Calculated and experimental neutron spectra in the atmosphere for various global conditions. The values of $d$ and $r_c$ are the atmospheric depth and the cutoff rigidity, respectively, while $s_{\min}$ and $s_{\max}$ indicate the solar minimum and maximum, respectively. [Sato and Niita, 2006]	13
2.1	Neutron absorption cross sections by $^3\text{He}$ , $^6\text{Li}$ , and $^{10}\text{B}$ . In grey the thermal and epithermal part of neutron spectrum is plotted.	20
2.2	energetic component of the response function for different detector types.	21
2.3	Detected neutron intensity over distance between origin and detector, for different soil moisture contents and humidity of $10 \text{ g/m}^3$ . Curves obtained from Monte Carlo Simulations [M. Köhli et al., 2015].	22

2.4	Calculated footprint (contour lines) dependency on soil moisture $\theta$ and humidity $h$ at sea level [M. Köhli et al., 2015] . . . . .	23
2.5	Penetration depths in the footprint as a function of radial distance from the sensor for exemplary soil moisture values $h$ . Obtained via Monte Carlo simulations . . . . .	23
2.6	Schematic representation of current and potential electrode in ERT technique. . . . .	24
2.7	Top: Wenner electrode configuration. Bottom: dipole.-dipole configuration . . . . .	26
2.8	Left: schematic of transmitter-receiver configuration. Right: primary and secondary magnetic fields with phase shift. . . . .	30
3.1	Site location in Italy. . . . .	33
3.2	Area of the study site around Grignanello showing the regional geological map in 1:10.000 scale. To help the orientation, the site where the majority of the measurements were performed is covered by the greyscale map of the EMI data, and the central ERT line (L1a), which is 72m long, is also drawn in red. . . . .	34
3.3	Survey map showing the eight ERT lines from both campaigns, sample locations, and the CRNP position. In the background, the conductivity map obtained with the EMI inversion, corresponding to $\sim 1.25$ m (bgl). . . . .	36
3.4	Core sampling using a manual core drill (left); sample hole in the field (right). . . . .	38
3.5	Bulk density values from shallow and deep samples. No evidence of a density gradient or spatial pattern is observed. . . . .	39
3.6	Site location in Italy. . . . .	42
3.7	Representative distribution of reciprocal errors from ERT data. Reciprocal errors were generally below 2.5%. . . . .	43

3.8	(Starting from the top) Inversion results from profiles <i>L2a</i> , <i>L1a</i> , <i>L3a</i> , and <i>LT</i> processed using ResIPy. Filtered applied on reciprocal errors at 2.5%, and linear error model to find the regularization parameters	44
3.9	<i>Mini Explorer by GF Insturments</i> . Multi-coil system for the frequency domain electromagnetic method acquisition. Automatic sampling with active GPS recording was performed by covering the whole field. . . . .	45
3.10	Interpolated FDEM conductivity maps at selected depths, respectively: 0.25 m, 0.5 m, and 0.75 m (continued in Figure 3.11). . . . .	47
3.11	Interpolated FDEM conductivity maps at selected depths: 1.0 m and 1.25 m (continued from Figure 3.10). . . . .	48
3.12	2D Schematic (not to scale) of the 3D model setup and neutron transport processes. Neutrons are emitted from a source layer following an atmospheric energy spectrum, interact with soil via nuclear evaporation, and scatter through material layers before detection. The detector response depends on neutron energy, and environmental components are defined by adjustable material and density parameters. .	51
3.13	Parameter panel of URANOS GUI . . . . .	52
3.14	Source plateau example. With a source radius of 250, m, edge effects are visible, extending approximately 100, m inward from the boundary.	54
3.15	Neutron count (left) and normalized neutron count (right) as a function of VWC for two porosity conditions. The data exhibit a hyperbolic trend, as expected from theory. In the title the $R^2$ of the fit are written . . . . .	57
3.16	<b>Left:</b> EMI inversion map (1.25 m bgl), calibrated with a 40 cm-spacing 72-electrode ERT line and interpolated using kriging. <b>Right:</b> Example of grayscale PNG input used in URANOS to encode spatially variable porosity and soil water content. The map models the 500m $\times$ 500m field centred in the detector. . . . .	58

3.17	Figure summarizing, in an intuitive scheme, the several simulations performed for this section. On the right side, the homogeneous simulations were performed specifying the porosity used and the VWC investigated. On the left side, the specifics for the two regions, in one case covered with a superficial homogenous layer. . . . .	59
3.18	Normalized count–VWC curves for simulations with and without a 30 cm homogeneous top layer. Counts are plotted against the mean VWC of the two regions. . . . .	60
3.19	Normalized neutron counts for homogeneous configurations with 30% and 50% porosity. . . . .	61
3.20	Results of the conversion with CoRNy for heterogeneous simulations. The two curves correspond to the conversions performed using the bulk densities of the two regions. . . . .	63
3.21	Heterogeneous simulation conversion results compared with the model input values of the two regions. The upper panel shows the results of the conversion performed using the silty loam bulk density for the whole field $\rho_b = 1.43 \text{ g/cm}^3$ , whereas the lower panel with $\rho_b = 2.002 \text{ g/cm}^3$ . . . . .	64
3.22	Heterogeneous conversion results (as in Fig. 3.21) plotted together with the conversion results of the homogeneous cases. Upper panel: $\rho_b = 1.43 \text{ g/cm}^3$ ; lower panel: $\rho_b = 2.002 \text{ g/cm}^3$ . . . . .	65

# List of Tables

1.1	Basic physical properties of the neutron. [M. O. Köhli, 2019]	5
1.2	Classification of neutrons by kinetic energy and corresponding interaction distances [M. O. Köhli, 2019].	7
1.3	Number of collisions required to moderate neutrons from 2 MeV to 25 meV for the most abundant isotopes present in the land-atmosphere interface	15
2.1	Nuclear properties of common elements in terrestrial rocks. $n_{\text{col}}$ number of collision to thermalize a 1 – 2MeV neutron. Values taken from [Sears, 1992].	18
3.1	Samples location in plane coordinates. First line shows the cosmic ray neutron probe position while the labels in the first columns were used to name the sample according to direction (N-North, S-south and so on) with respect to the detector position and the number is just sequential, considering that for every location two soil samples were collected odd numbers are for shallow samples and even for deep. Bulk density values in $\text{kg}/\text{m}^3$ and VWC in percentage for all 13 samples.	40
3.2	Mass loss percentages from LOI analysis at $450^\circ\text{C}$ , used to estimate organic matter content in selected samples.	41
3.3	Summary of the ERT lines performed during both field campaigns. The table provides line name, length, electrode spacing, number of roll-on segments, acquisition direction, and relative position with respect to line L1a, which is the central S–N profile located near the CRNP.	43

3.4	Neutron footprint and depth ( $z_{86}$ ) for simulations with $5 \cdot 10^7$ neutrons under two different porosity scenarios. . . . .	55
3.5	Geometrical and physical parameters representative of the Borgo Grignanello site, shared by all simulations. . . . .	56
3.6	Heterogeneous simulation configurations. Porosity is set to 30% in Region 1 and 50% in Region 2. All simulations were also repeated with a 30 cm homogeneous top layer. . . . .	59
3.7	Conversion results from CoRNy for homogeneous simulations corresponding to the two regions of the heterogeneous setup (Region 1, marl; Region 2, silty loam). The first row reports the VWC values used as input in the Monte Carlo ground model. . . . .	62
3.8	Conversion results from CoRNy for heterogeneous simulations. The first row reports the VWC inputs assigned to the ground model (Region 1 – Region 2). . . . .	63

# Glossary

**CRNS** Cosmic Ray Neutron Sensing. 1

**CZ** Critical Zone. 1

**EMI** Electromagnetic Induction (method). 3

**ERT** Electrical Resistivity Tomography. 3

**ET** Evapotranspiration. 58

**FDEM** Frequency Domain Electromagnetic induction Method. 3

**LOI** Loss on ignition. 41

**RWU** Root Water Uptake. 58

**SWC** Soil Water content. 1

**WC** Water Content. 19



# Introduction

The Earth's Critical Zone (CZ), extending from the plant canopy to the base of the aquifers, is the domain in which fundamental processes regulate the exchange of water, energy and nutrients. Within this framework, the vadose zone plays a pivotal role in mediating the interactions between soil, vegetation, and the atmosphere [Casiani et al., 2015, Binley et al., 2015]. The processes that occur in this unsaturated zone directly affect pressing environmental and agricultural issues, ranging from the availability of water for crops to slope stability and the mitigation of flood risk [Uhlemann et al., 2024]. In agricultural systems in particular, root water uptake, soil evaporation, and infiltration are critical processes for sustaining productivity, especially under changing climatic conditions.

A central challenge in hydrological and environmental sciences is the accurate quantification of soil water content (SWC) across scales. Reliable SWC estimates are essential to improve hydrological models, support irrigation management, and refine climate and land surface schemes. Current methods, however, face scale-related limitations: point sensors provide highly localized measurements, whereas remote sensing offers broad coverage but at coarse resolution, often missing the intermediate scales most relevant for field-scale water management.

In recent years, Cosmic-Ray Neutron Sensing (CRNS) has emerged as a promising technique that naturally bridges this observational gap [Desilets et al., 2010, Zreda et al., 2012, M. O. Köhli, 2019, Wang et al., 2025]. The technique monitors the above-ground flux of cosmic-ray neutrons, which is inversely related to the hydrogen content of the surrounding environment. Since its first introduction by [Zreda et al., 2008], CRNS has gained steady recognition within the hydrological sciences as a reliable tool for soil moisture monitoring. Its widespread adoption stems from

a series of distinct advantages. Unlike point sensors, CRNS integrates soil moisture information over a comparatively large footprint, typically 10–20 hectares, with penetration depths reaching up to 80 cm, thereby capturing field-scale variability. It operates passively and non-invasively, with the practical advantage of being largely autonomous: probes are often solar-powered, require minimal maintenance, and can be readily combined with other environmental monitoring systems [M. O. Köhli, 2019]. Importantly, the detected signal is solely dependent on the environmental hydrogen content, irrespective of its phase, and offers a temporal resolution ranging from minutes to a few hours depending on sensor configuration. In addition, mobile applications of CRNS have demonstrated the capacity to extend its spatial coverage across tens of square kilometers, providing unique opportunities for regional-scale investigations [Schrön et al., 2018].

Nevertheless, it is essential to recognize that CRNS is not a straightforward tool. It is a highly interdisciplinary technique, sitting at the crossroads of geography, hydrology, and neutron physics. While the method has made considerable progress in its first decade of development, roughly between 2008 and 2018, it has been advanced by a relatively small research community [Weimar, 2022]. As a result, several fundamental questions remain unresolved, particularly regarding calibration procedures, environmental corrections, and the interpretation of signals in complex, heterogeneous landscapes. These challenges frame the context in which this thesis is situated. The interest towards the technique rapidly developed within the hydrological community, with applications ranging from irrigation scheduling to the validation of land-surface models. However, challenges remain in translating neutron counts into accurate water content, particularly under heterogeneous soil and lithological conditions.

This thesis is positioned within this evolving field to advance the understanding and application of CRNS by combining numerical neutron transport simulations with field-scale geophysical and hydrological investigations. Specifically, it explores the basics of the technique as well as how soil heterogeneity influences neutron dynamics and how additional geophysical information can improve the interpretation of CRNS.

---

The first part of this work (Chapter 1) will be dedicated to providing an overview of the theoretical background on cosmic-ray neutrons, introducing the physical principles underlying neutron generation, interactions, and in particular, moderation.

An overview of the working mechanism of the CRNS technique is provided in Chapter 2. The research focused on the neutron acquisition method and detection features, such as radial footprint and penetration depth. Subsequently, the theory behind the more common geophysical measurement techniques, such as Electrical Resistivity Tomography (ERT) and Frequency Domain Electromagnetic induction method (FDEM or EMI) will be briefly discussed. These methods were chosen for the field investigation as representative of the state of the art for near-surface and hydro-geophysics [Cassiani et al., 2016, Binley et al., 2015].

The bulk density of the soil present at the site represents a necessary information for the instrument and conversion software configurations; moreover, the CRNP product needs to be calibrated on a dataset corresponding to known VWCs. For this reason, soil sampling was performed according to [Schrön et al., 2017]. The procedure, as well as the analysis performed, are also reported in this chapter.

A short description of the site introduces the next chapter. The outline of the study area focuses on the geological and pedological features of the area, as well as providing an overview of the morphology of the surroundings. Worth describing is also the vegetation and the environmental context of the vineyard test area, where measurements were conducted.

Chapter 3 dives into the core of the work, describing the field data acquisition and the related processing, leading to the modeling and Monte Carlo simulations. These were performed to go in depth into the understanding of the particles' behaviour under different site conditions and in particular, the effect of the field heterogeneity, aiming to model the real site. This study is of fundamental importance for enhancing the interpretation capabilities and to prove the necessity of a combined approach with the support of geophysical investigation.

Eventually, in Chapter 4, the results obtained from the samples and the geophysical surveys, as well as the outcomes of the simulation work, will be presented and critically discussed. The latter provide consistent and promising insights, laying a

## INTRODUCTION

---

base for further investigations, and providing sparks for making the approach more robust.

# Chapter 1

## Cosmic-ray neutrons

### 1.1 The neutron

Mass	1.00866491588(5) u 939.565413(6) MeV/c <sup>2</sup>
Spin	1/2 $\hbar$ /2 $\pi$
Mean Lifetime	879.6 (8)s
Mean-square charge radius	-0.1161(22)fm <sup>2</sup>
Magnetic moment	-1.91304273(45) $\mu_N$

Table 1.1: Basic physical properties of the neutron. [M. O. Köhli, 2019]

The neutron is a subatomic particle with zero net charge and spin  $1/2\hbar$ , where  $h$  and  $\hbar = h/2\pi$  are the Planck and reduced Planck constant, respectively <sup>1</sup>. Its rest mass is slightly higher than that of the proton, which allows it to decay weakly into a proton, an electron, and an electron antineutrino:



with a maximum kinetic energy transfer of 781.32 keV and a mean lifetime of approximately 15 minutes [Paul, 2009]. As a result, free neutrons are almost absent in the universe; the only stable condition is the bound state within the atomic nucleus.

---

<sup>1</sup>The Planck constant is a fundamental physical constant, value  $6.62607015 \cdot 10^{-34} \text{J Hz}^{-1}$ ,  $\hbar$  is called the reduced Planck constant, corresponding to  $h/2\pi$

### 1.1.1 Neutron Energies

The neutron energy, often referred to as the neutron “temperature,” describes the kinetic energy  $E$  of a free neutron (usually expressed in electronvolts, eV) and primarily determines its interaction with matter. In the non-relativistic limit, the neutron’s kinetic energy can be expressed through its de Broglie wavelength  $\lambda_B$ :

$$\lambda_B = \frac{h}{m_n v} \quad \rightarrow \quad E = \frac{1}{2} m_n v^2 = \frac{h^2}{2m_n \lambda_B^2} \quad (1.2)$$

where  $h$  is the Planck constant, and  $v$  and  $m_n$  are the velocity and rest mass of the neutron, respectively.

The classification of neutron energies is given in Table 1.2. The terminology derives from the temperature  $T$  of the medium with which the neutrons are in thermal equilibrium. According to the kinetic theory of ideal gases, the energies  $E$  of the particles in the system follow a Maxwell–Boltzmann distribution:

$$f_E(E) = 2\sqrt{\frac{E}{\pi}} \left(\frac{1}{k_b T}\right)^{3/2} e^{-\frac{E}{k_b T}} \quad (1.3)$$

where  $k_B$  is the Boltzmann constant <sup>2</sup>.

The most probable neutron energy  $E_n$ , corresponding to the maximum of this probability density function, is related to temperature by:

$$\frac{df_E(E)}{dE} = 0 \quad \rightarrow \quad T = \frac{E_n}{k_B} = \frac{m_n v_n^2}{2k_B} \quad (1.4)$$

In the context of this work, neutrons with energies lower than the thermal regime are not considered.

### 1.1.2 Neutron interactions

Neutron interactions are governed primarily by the nuclear force. Because nucleon potentials extend only over a few femtometers, the de Broglie wavelength of the neutron largely determines the range of interaction. At energies above the thermal regime, the short wavelength of neutrons reduces the interaction time with the

---

<sup>2</sup>The Boltzmann constant is the proportionality factor that relates the average relative thermal energy of particles in a gas with the thermodynamic temperature of the gas, value  $1.380649 \cdot 10^{-23} \text{ J K}^{-1}$

	Kinetic energy [eV]	Velocity [m/s]	Wavelength [Å]
Ultra cold	$< 3 \cdot 10^{-7}$	$< 7.5$	$< 520$
Very cold	$3 \cdot 10^{-7} - 5 \cdot 10^{-5}$	$7.5 - 100$	$520 - 40$
Cold	$5 \cdot 10^{-5} - 5 \cdot 10^{-3}$	$100 - 1000$	$40 - 4$
Thermal	$5 \cdot 10^{-3} - 5 \cdot 10^{-1}$	$1000 - 10000$	$4 - 0.4$
Thermal peak	$25.3 \cdot 10^{-3}$	$2200$	$1.8$
Epithermal	$5 \cdot 10^{-1} - 5 \cdot 10^3$	$10^3 - 4.4 \cdot 10^5$	$0.4 - 0.01$
Intermediate	$10^3 - 10^5$	$4.4 \cdot 10^5 - 4.4 \cdot 10^6$	$0.01 - 0.001$
Fast	$10^5 - 2 \cdot 10^7$	$4.4 \cdot 10^6 - 6.2 \cdot 10^7$	$0.001 - 6 \cdot 10^{-5}$
High energy	$> 2 \cdot 10^7$	$> 6.2 \cdot 10^7$	$< 6 \cdot 10^{-5}$

Table 1.2: Classification of neutrons by kinetic energy and corresponding interaction distances [M. O. Köhli, 2019].

nucleus, lowering the probability of interaction. Consequently, neutrons can often travel long distances in matter without interacting.

The probability of interaction is quantified by the cross section  $\sigma$ , expressed in units of area [ $L^2$ ], usually in barns ( $1 \text{ barn} = 10^{-24} \text{ cm}^2$ ). Intuitively, it can be considered as an effective area surrounding a particle, where a larger area corresponds to a higher probability of interaction. Cross sections typically reflect the geometric size of the nucleus and depend strongly on the neutron's energy [Forget et al., 2010].

The total cross section  $\sigma_t$  is the sum of the contributions from scattering and absorption processes.

Two general types of neutron interactions can be distinguished, usually denoted as  $(n, X)$  reactions, where  $n$  is the incident neutron and  $X$  the reaction product <sup>3</sup>: **Scattering**, in which the neutron changes speed and/or direction but the target nucleus retains the same proton and neutron numbers. This includes *elastic*, *inelastic*, *resonance*, and *coherent* scattering. **Absorption**, where the neutron is captured and a compound nucleus is formed. The excited nucleus then de-excites by emitting one or more particles  $X$  (photons, neutrons, or charged particles).

Elastic scattering  $(n, n)$  is the dominant energy-loss mechanism, akin to a classi-

<sup>3</sup>Also the apostrophe, is used to indicate neutrons with different energies, and the star, for example in  $(A, Z)^*$  indicates an excited state of the nucleus

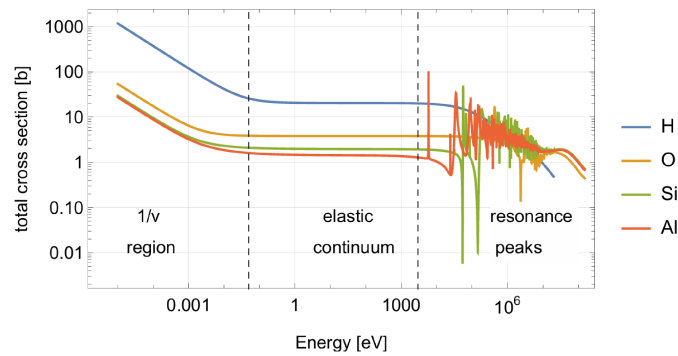


Figure 1.1: Total cross section in barns for the interaction of neutrons with hydrogen (blue), oxygen (orange), silicon (green), and aluminum (red).

cal billiard-ball collision with conservation of energy and momentum in the center-of-mass of the system. Inelastic scattering ( $n, n'(+X)$ ) occurs when part of the neutron's kinetic energy excites the nucleus, possibly leading to the emission of additional products. Resonance scattering ( $n, n/n'$ ) arises when the neutron energy matches nuclear excitation levels, producing sharp resonance peaks in cross sections.

Absorption processes include: *Radiative capture* ( $n, \gamma$ ), where the compound nucleus emits a photon; *Charged particle emission* ( $n, p/d/\alpha$ ), where protons, deuterons, or alpha particles are released; *Neutron multiplication* ( $n, 2n$ ) or ( $n, 3n$ ); *Fission*, relevant for heavy nuclei, where the absorption of a slow neutron leads to splitting into fragments with additional neutron emission.

At very high energies ( $> 100$  MeV), spallation can occur, in which the nucleus is fragmented by the projectile, producing multiple secondary particles.

A key concept for this work is the dependence of the cross section on energy. Figure 1.1 shows the energy-dependent total cross sections of hydrogen, oxygen, silicon, and aluminum, the most abundant isotopes at the atmosphere-land interface. Three main regions can be distinguished: the  **$1/v$  region** (thermal energies), where cross sections scale inversely with neutron velocity due to longer interaction times. The **resonance region**, dominated by sharp peaks associated with nuclear excited states. The **fast-neutron region**, where cross sections remain relatively constant and elastic scattering dominates.

The angular dependence of interactions is described by the differential cross section

$\frac{d\sigma}{d\Omega}$ , whose integration over  $4\pi$  steradians yields the total cross section:

$$\sigma_t = \oint_{4\pi} \frac{d\sigma}{d\Omega} d\Omega \quad (1.5)$$

For materials, the concept of a *macroscopic cross section* is often used:

$$\Sigma(E) = \sum_{i=1}^N n_i \sigma_{i,t}(E) \quad (1.6)$$

where  $n_i$  is the number density and  $\sigma_{i,t}$  the total microscopic cross section of isotope  $i$ . Its inverse defines the mean free path  $L(E)$ :

$$L(E) = \frac{1}{n\sigma_t(E)} = \frac{1}{\Sigma(E)} \quad (1.7)$$

Finally, when a beam of neutrons passes through matter, its intensity decreases exponentially with depth, following the Beer–Lambert law [Horvath, 1988]:

$$I(d) = e^{-d/\lambda} \quad (1.8)$$

where  $d$  is depth and  $\lambda$  the attenuation length, which depends on the density  $\rho$  of the medium.

## 1.2 Neutrons origin

### 1.2.1 Primary cosmic-rays

Cosmic rays can be subdivided into *primary cosmic rays*, *secondary cosmic rays*, *solar cosmic rays*, and *terrestrial cosmic rays*. In this context the attention is driven towards the first two.

The primary cosmic rays are defined as: galactic particles which enter the solar system and may hit the earth [Ziegler, 1996]. They are believed to be produced and accelerated as a consequence of stellar flares, supernova explosions, pulsars, and the explosion of galactic nuclei. Because of their vast spiraling trajectory<sup>4</sup> a local observer perceives the particle income as isotropic. Primary cosmic rays are almost

<sup>4</sup>Because our galaxy is spinning, there is a pervasive magnetic field of several micro-Gauss, and the cosmic rays interact with this field so that, typically, they spiral continually during their lifetime with a spiral diameter of a fraction of the galactic diameter.

exclusively charged particles: 92% are protons and 6% are alpha-particles, the rest is made of heavier atomic nuclei. Thus, they are subject to the Lorentz force when directed at the Earth inflicted by its magnetic field, which at first order has dipole structure tilted by 11 degrees with respect to rotation axis.

$$\frac{d\mathbf{v}}{dt} = \frac{q}{\gamma m} \cdot \mathbf{v} \times \mathbf{B}(\mathbf{r}) \quad (1.9)$$

where  $\gamma = 1/\sqrt{1 - v^2/c^2}$  is the Lorentz factor. The effect of the force is to deflect and reflect the charged particles, especially the low energetic ones. The maximum effect happens when the trajectory of the particle is perpendicular to the field, while there is not effect on charged particles entering vertically into the poles. In general, depending on the inclination angle to the field a particle spirals around the field lines with a radius  $r$ :

$$q\mathbf{v} \times \mathbf{B}(\mathbf{r}) = \gamma \frac{\mathbf{v}^2}{r} \quad (1.10)$$

which in scalar form writes:

$$Br = \frac{\gamma m v}{q} = \frac{p}{q} \quad (1.11)$$

using the momentum  $p$  of the particle. The quantity  $Br$  is called *magnetic rigidity* and can be expressed in GV (gigavolts). The effectiveness of the earth's magnetic shield in preventing sea-level cosmic showers is discussed in terms the magnetic rigidity, in fact, depending on incoming direction and destination location there is an energy threshold, called cutoff rigidity  $r_c$ , below which the particle flux on the ground, due to magnetic shielding, becomes zero.

Since the primary protons, which can cause a sea-level shower, are all highly relativistic, we can simplify this discussion by assuming their energy to be the same as their rigidity, but with the units changed from eV to V [Ziegler, 1996]. Near the magnetic poles, where the geomagnetic field is nearly vertical, the cutoff rigidity approaches zero, and the maximum number of primary cosmic rays can reach the atmosphere. As a result, cosmic-ray neutron amount (which in this case can be seen as a proxy for cosmic ray particles amount) is highest in polar regions and decreases toward the equator, see fig 1.2. The size of this effect depends on altitude and the time in the solar cycle. In fact, the sun has a varying magnetic field with a basic dipole component that reverses direction approximately every 11 years and

might affect the charged particle flux. Near reversals, at “solar maximum,” there are many sunspots and other manifestations of magnetic turbulence, and the plasma of protons and electrons ejected from the sun (the solar wind) carries a relatively strong and convoluted magnetic field with it outward through the solar system. At solar maximum, primary cosmic rays are maximally deflected as they enter the solar system, causing a radiation minimum at Earth. The opposite happens at “solar minimum,” where there are few sunspots, so this is the time of maximum radiation.

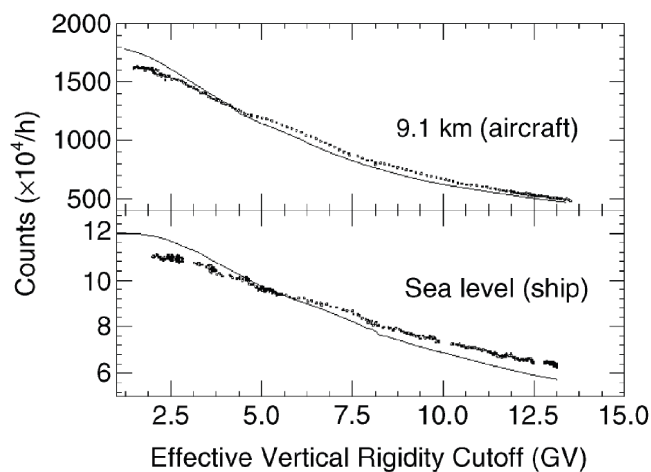


Figure 1.2: The effect of the Earth’s magnetic field on cosmic-ray neutron intensity is shown by graphs of count rate as a function of geomagnetic vertical cutoff rigidity for a cosmic-ray neutron monitor (dots) [Goldhagen, 2003]. The curves are calculated [Clem and Dorman, 2000].

### 1.2.2 Secondary cosmic rays

The net charge of the cosmic ray radiation is highly positive, with protons dominating the particle population. The cosmic ray spectrum extends from the MeV regime up to ZeV energies, see Figure 1.3.

Cosmic ray particles that are energetic enough to travel through the magnetic fields enter the atmosphere where they collide with and disintegrate nuclei to create energetic secondary particles, which in turn produce tertiary particles in a chain reaction. In this work we refer to *secondary cosmic ray* as the particle fluxes constantly produced when primary cosmic rays collide with the atmosphere and soil below.

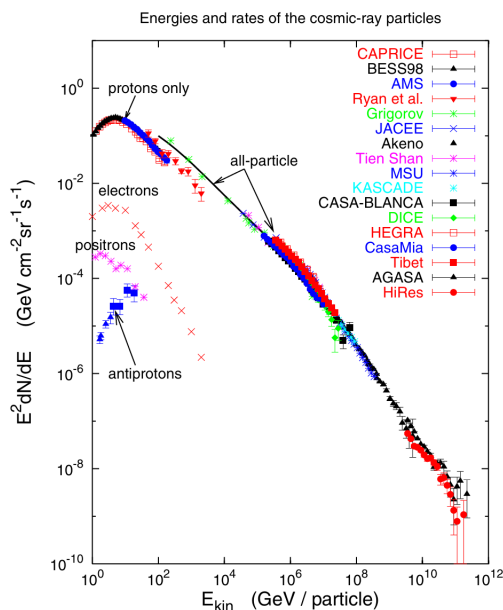


Figure 1.3: Global view of the primary cosmic ray spectrum obtained studying the produced cascades in the atmosphere with detectors on the ground that have large effective area for sampling such showers. [Gaisser, 2006]

Neutrons in particular can be generated only by releasing them from nuclei. The different mechanisms leading to this to happen are beyond the scope of this work. Figure 1.4 indicates how primary galactic cosmic-rays (protons,  $\alpha$  particles and others) are attenuated by the atmospheric mass. Their attenuation leads to the production of secondary cosmic-rays inside the particle showers as: neutrons, electrons, photons, and muons; note that this list is not complete as many hadronic particles are produced to a lesser extend in the cascades. In the upper layers of the atmosphere the flux of secondary cosmic rays increases to higher depth because the primary flux that sources the secondary flux is still large. Their intensity peaks at the Pfozter maximum<sup>5</sup>, see Figure 1.4. Below that the particle loss due to the propagation through the atmospheric medium overcomes the source term. Although neither being present in cosmic radiation nor being the dominant production channel neutrons make up a large part of the particles at ground level as their interaction probability is smaller compared to charged particles and their lifetime is long enough to traverse the atmosphere. The neutron density increases by spallation reactions in the upper atmosphere, and beyond the Pfozter maximum it follows a simple

<sup>5</sup>found at around (50–100) g/cm<sup>2</sup>, ca. 20km, atmospheric depth according to Pfozter, 1936, while Nesterenok, 2013 inferred a value of (30–150) g/cm<sup>2</sup>

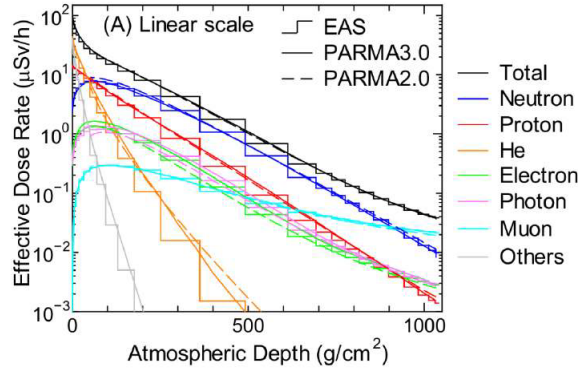


Figure 1.4: Atmospheric depth dependencies of effective dose rates at  $r_c = 0$  GV and solar minimum conditions [Weimar, 2022]

exponential law as a function of atmospheric depth.

### 1.2.3 Neutron spectrum above the soil and modulation

The cosmic ray neutron spectrum above the land-atmosphere interface can be seen in Figure 1.5, the present features are based on the physics that lies behind the different production processes.

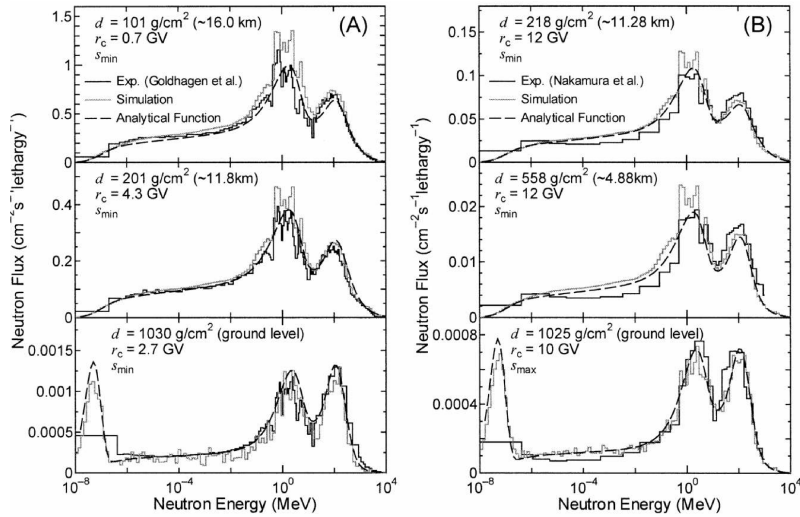


Figure 1.5: Calculated and experimental neutron spectra in the atmosphere for various global conditions. The values of  $d$  and  $r_c$  are the atmospheric depth and the cutoff rigidity, respectively, while  $s_{\min}$  and  $s_{\max}$  indicate the solar minimum and maximum, respectively. [Sato and Niita, 2006]

From epithermal up to fast, neutrons primarily scatter elastically when interacting with nuclei. Moreover, their energy is high enough to assume the target nuclei to

be at rest. Thus, during their propagation, neutrons are subject to slowing down, this energy loss is called *moderation*. How effective this process is, depends on the *moderation power* of the material itself. Up to these energy levels the study of the collision processes can still be treated non-relativistically.

By elastic collisions always a fraction of the kinetic energy is lost, and this is expressed in terms of lethargy  $u = \ln \frac{E_0}{E}$ , which describes the logarithmic energy loss for a single scattering event.

Assuming isotropic scattering it is useful to consider the average energy lethargy  $\xi = \overline{u(\theta)}$  (being  $\theta$  the deflection angle). Therefore, the moderation power of a material can be expressed through the average number of collisions  $n_{\text{col}}$  needed to decelerate neutrons from an initial energy  $E_0 = \frac{1}{2}mv_0^2$  to a certain final energy  $E_f$  as for instance the energy down to the thermal regime (25 meV).

$$n_{\text{col}} = \frac{u}{\xi} \quad (1.12)$$

This property of the material decreases with nuclide mass, and the slowing down requires more collisions. In fact, the energy of the scatterer neutrons is limited within the range:

$$\left( \frac{A-1}{A+1} \right) E_0 < E < E_0 \quad (1.13)$$

where  $A$  is the mass of the interaction partner, generally expressed as a multiple of the neutron's mass. Therefore, if the neutron is scattering at a nucleus with similar mass  $A = 1$ , it follows  $0 < E < E_0$ , which means that the entire kinetic energy of the neutron is transferred to the nucleus in head-on neutron-proton collisions.

To describe a mixed-isotope material, the the average lethargy for each isotope need to be combined, weighted for their elastic scattering cross section  $\sigma_i$

$$\overline{n_{\text{col}}} = \ln \frac{E_0}{E} \left( \frac{\sum_i \sigma_i \xi_i}{\sum_i \sigma_i} \right)^{-1} \quad (1.14)$$

To conclude, it is interesting to check the table below Table 1.3 to see the moderation power related to the most abundant isotopes around the land-atmosphere interface, taken from [M. Köhli et al., 2021]. In this case, the average collision number represents the collisions required to moderate from 2 MeV to 25 meV.

Isotope	Mass [u]	$\xi$	$\bar{n}_{\text{col}}$
H	1	1	18
H <sub>2</sub> O	-	0.92	20
N	14	0.134	135
O	16	0.12	153
Al	27	0.0723	255
Si	28	0.0698	264
Fe	56	0.0353	522
SiO <sub>2</sub>	-	0.11	166
Air (dry)	-	0.135	135

Table 1.3: Number of collisions required to moderate neutrons from 2 MeV to 25 meV for the most abundant isotopes present in the land-atmosphere interface



# Chapter 2

## Background on geophysical investigation methods

This chapter will present the geophysical methods used in this work. The first part will be devoted to the cosmic ray neutron sensing technique, followed by electrical resistivity tomography (ERT) and the frequency domain electromagnetic induction method (FDEM or EMI).

### 2.1 Cosmic Ray Neutron Sensing

#### 2.1.1 Principles of the method

The previous chapter aims to give a superficial overview of the formation and propagation of free neutrons in the atmosphere. Thanks to their neutral charge, and thus relatively long life, and mass, these particles are suitable for environmental purposes. The idea behind CRNS is to use epithermal neutrons as a proxy for ambient hydrogen content. Comparing neutron spectra above dry to wet soil reveals a strong intensity decline with soil moisture increase in the epithermal regime [Weimar, 2022].

Fast neutrons that are produced undergo elastic collisions in the atmosphere, water, and vegetation, and lose energy until they are eventually absorbed in inelastic nuclear collisions (since they are not stable particles in nature). The moderation

Element	A	$\sigma$ [barns]	$n_{\text{col}}$	$\xi$	SP [ $\text{cm}^{-1}$ ]	C [ppm]
H	1.00	22.02	18	1.000	22.016	-
O	16.00	4.232(6)	149	0.120	0.508	487 875
C	12.01	5.55	113	0.158	0.875	87 638
Si	28.09	2.167	257	0.070	0.151	281 367
Fe	55.85	11.62	505	0.035	0.411	28 980

Table 2.1: Nuclear properties of common elements in terrestrial rocks.  $n_{\text{col}}$  number of collision to thermalize a 1 – 2MeV neutron. Values taken from [Sears, 1992].

process mainly depends on: the probability of scattering by different elements is determined by the microscopic cross section; the number of nuclei of different elements, or the elemental concentration (which, together with the previous factor, determines the macroscopic cross section), and the energy loss per collision, also called lethargy  $u$ . Table 2.1 integrates Table 1.3 with the elemental cross section, the elemental stopping power (SP) calculated as  $\xi \cdot \sigma_i$  and C, the concentration in ppm, of a few elements found also in [Zreda et al., 2012].

CRNS relies on the fact that hydrogen is by far the most efficient element in moderating fast neutrons. Because of its large cross section and mass similar to neutrons, the latter will transfer much of its energy to the hydrogen proton, so the kinetic energy lost is much. In particular, as shown in table 2.1, the moderation capability of hydrogen and water is on average one order of magnitude larger than that related to the other isotopes populating the zone of interest.

To appreciate the reduction of epithermal neutrons as a function of hydrogen content, it is useful to consider the equilibrium concentration of fast neutrons above the ground surface as how many are produced and how many are moderated to lower energies. Neutron intensity above the surface is inversely correlated with soil moisture, in fact:

$$\phi(E) = \frac{Q}{E \cdot \text{SP}} \quad (2.1)$$

$$= \frac{Q}{E \cdot \sum_{i=1}^n (N_i \cdot \sigma_i \cdot \xi_i)} \quad (2.2)$$

$$= \frac{Q}{E \cdot (N_H \cdot \sigma_H \cdot \xi_H + \sum_{i=2}^n (N_i \cdot \sigma_i \cdot \xi_i))} \quad (2.3)$$

where  $\phi$  is the intensity of the neutrons of energy  $E$ ;  $Q$  is the intensity of the source of the neutrons (number of fast neutrons produced); and SP is the macroscopic

stopping power of a material (where the upper boundary  $n$  is the number of relevant elements in the soil).

$Q$  is known implicitly from calibration on local soil or theoretical computation [Zreda et al., 2012], and  $\phi$  is measured; therefore, the equation 2.1 can be solved for  $SP$ , but since  $SP_H$  (of hydrogen) dominates 2.1, the number of hydrogen atoms in the soil,  $N_H$ , can be inferred. Eventually, hydrogen can be directly linked to the soil moisture  $\theta$  through the semi-empirical relation [Desilets et al., 2010] 2.4, which shows a hyperbolic dependency.

$$\theta(N) = \rho_b \left( \frac{a_0}{\left(\frac{N}{N_0}\right) - a_1} - a_2 \right) \quad (2.4)$$

With  $\theta$  being the volumetric water content,  $\rho_b$  the soil's bulk density (used to convert from gravimetric to volumetric WC);  $N$  is the neutrons detector counting rate normalized to a reference atmospheric pressure and solar activity level [Desilets et al., 2010];  $N_0$  is site and neutron detector specific, and demands for a single calibration measurement [Schrön et al., 2017]; while  $a_i$  are fitting parameters deduced as  $(a_0, a_1, a_2) = (0.0808, 0.372, 0.115)$  from an empirical analysis in [Desilets et al., 2010].

It is important to mention that fast neutrons are also produced and moderated in the atmosphere, and small variations in the water vapor content affect the fast neutron intensity; hence, a correction for atmospheric moisture content should be included. For these reason, a revised version of equation 2.4 was published in 2021, found by combining the influence of soil and atmospheric moisture, including the latter using a linear function, which has been proposed as the *universal transport solution (UTS)* [M. Köhli et al., 2021].

## 2.1.2 Cosmic ray neutron detector

Generally, particle detectors rely on the interaction of the particle with an appropriate detection substance, and the energy change triggered by this reaction is recorded. Efficient neutron detectors almost exclusively rely on neutron converters: Evapora-

tion<sup>1</sup> and epithermal neutrons may be detected indirectly by light recoil nuclei via elastic scatter, which in turn induces an ionization signature within the detection volume. However, the efficiency for detecting neutrons by elastic scattering is around two orders of magnitude lower than the efficiency for absorption of thermal neutrons [Weimar, 2022]. Therefore, neutron converters have a high probability of inducing a strong ionization signal via neutron absorption. However, as was discussed above, absorption processes are only significant in the thermal energy regime; therefore, detectors that rely on such converters are called thermal neutron detectors. The most relevant isotopes also for CRNS purposes are the one shown in Figure 2.1:  $^3\text{He}$ ,  $^6\text{Li}$ , and  $^{10}\text{B}$ .

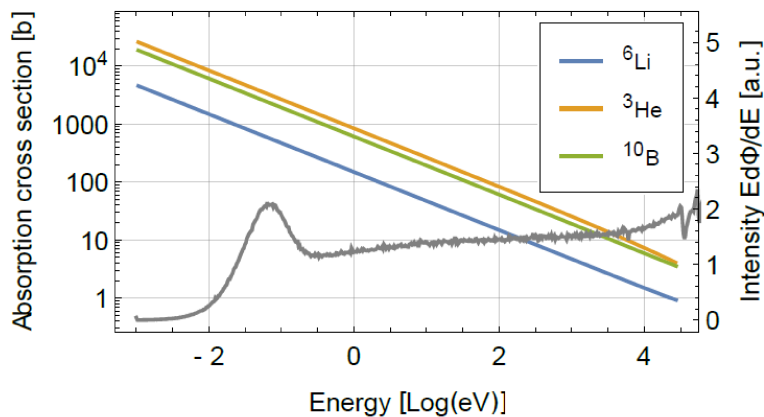


Figure 2.1: Neutron absorption cross sections by  $^3\text{He}$ ,  $^6\text{Li}$ , and  $^{10}\text{B}$ . In grey the thermal and epithermal part of neutron spectrum is plotted.

The output of cosmic-ray neutron detectors is a count of the detected neutrons per second. The detector can be set to acquire with a certain time window and store the data into files. They are generally provided with some the basic sensors, for instance, temperature and pressure sensors which might turn out to be useful for conversion corrections.

Detector performance is typically described by an response function, representing the system's sensitivity to incident particles as a function of both their energy and angle of incidence. In the investigation conducted by [M. Köhli et al., 2018], this energy-dependent neutron response was quantified via Monte Carlo simulations across a

<sup>1</sup>The term originates from the production mechanisms of the neutron; it corresponds to fast and intermediate neutrons

variety of detector configurations. The analysis depicted in Figure 2.2 reveals that all models exhibit comparable qualitative behavior over the energy interval from 0.1eV to 1MeV, with a distinct response peak occurring between 1eV and 10eV. Variations in the absolute detection efficiency, arising from differences in detector architecture, converter gas composition, and casing geometry, account for the primary discrepancies observed among the models.

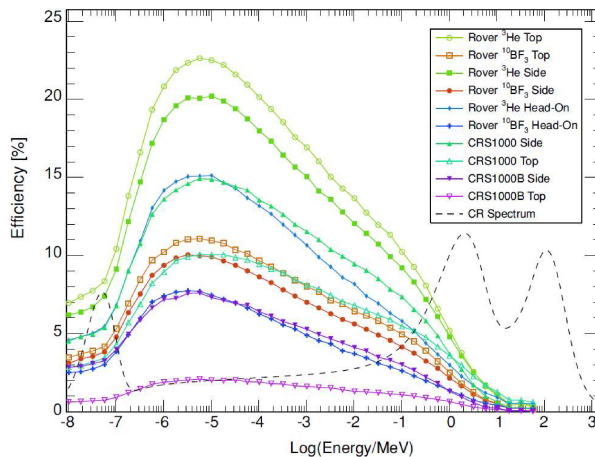


Figure 2.2: energetic component of the response function for different detector types.

The dependence from the incident angle shows higher sensitivity to orthogonal fluxes, this result stresses the importance of accounting for neutron fluxes directly from atmospheric cosmic rays and from beneath the sensor [M. Köhli and Weimar, 2024].

### 2.1.3 Footprint and penetration depth

We define the area of influence (lateral footprint) as a radially symmetric region contributing a specific, arbitrarily large fraction of the counting rate to a centrally located sensor. When a sensor is centrally located and detects neutrons isotropically, it creates a scenario with point symmetry, leading us to assume a circular footprint. In this context, the footprint is defined as the radius of the circle where 86% of the detected neutrons make their initial contact with the ground.

Figure 2.3 illustrates how the detected neutron intensity decreases radially; it can be noticed that the response doesn't follow a simple exponential trend.

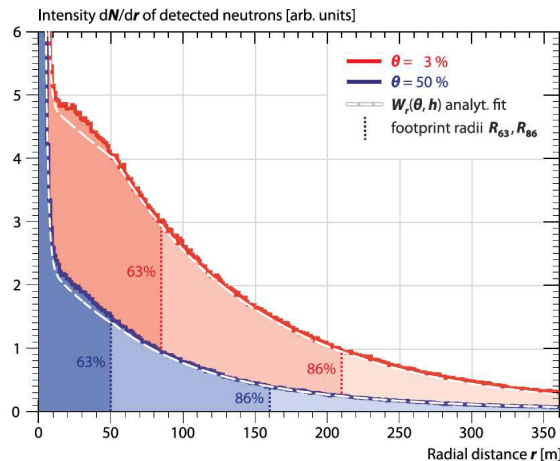


Figure 2.3: Detected neutron intensity over distance between origin and detector, for different soil moisture contents and humidity of  $10 \text{ g/m}^3$ . Curves obtained from Monte Carlo Simulations [M. Köhli et al., 2015].

The elevated signal at radii less than 10 meters ( $r < 10 \text{ m}$ ) originates from neutrons directly emitted by the ground. These neutrons, despite predominantly having lower energies, have a high probability of detection. The region extending up to 50 meters ( $r < 50 \text{ m}$ ) primarily reflects the average mean free path of most environmental neutrons in humid air. Beyond this, for distances between 50 and 200 meters, neutrons undergo multiple interactions with the soil before detection. This signifies that as the radial distance increases, the average neutron energies rapidly become insufficient for them to reach the detector before thermalization. From approximately 200 meters onward, the detected neutrons are predominantly from the higher-energy portion of the spectrum. These higher-energy neutrons exhibit greater flux rates and are capable of probing the soil at significant distances from the detector.

The footprint is found to be strongly dependent on air humidity and soil moisture content. [Desilets and Zreda, 2013] investigated the influence of air humidity in detail and found the response to variations of absolute humidity features a 10 m decrease of the footprint radius for every change of  $\approx 6 \text{ g/m}^3$  water vapor; notice that air humidity from dry to saturated can easily span  $\approx 25 \text{ g/m}^3$ .

[M. Köhli et al., 2015] examined additional factors that contribute to footprint variability, like vegetation and air pressure, whose investigation is outside the purview of this paper.

Analogously, one can define a *penetration depth*. A notable advantage of the CRNS

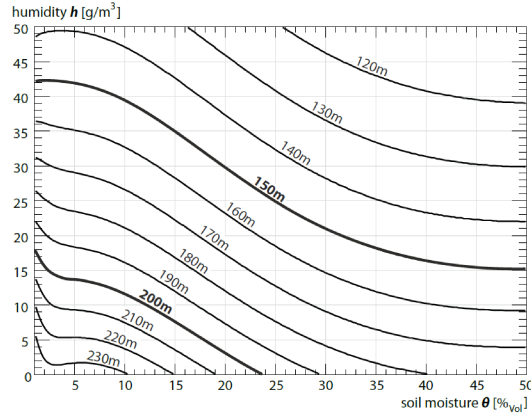


Figure 2.4: Calculated footprint (contour lines) dependency on soil moisture  $\theta$  and humidity  $h$  at sea level [M. Köhli et al., 2015]

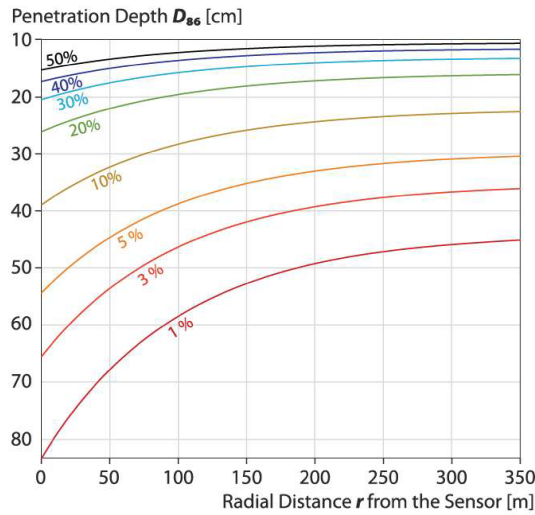


Figure 2.5: Penetration depths in the footprint as a function of radial distance from the sensor for exemplary soil moisture values  $h$ . Obtained via Monte Carlo simulations

method over most remote-sensing techniques is the thickness of the soil layer it probes. This is because cosmic-ray neutrons can penetrate the uppermost decimeters of the soil with minimal impedance. This quantity strongly depends on the soil moisture content (Figure 2.5): the penetration depth varies between 15 cm and 83 cm below the sensor for wet and dry soil, respectively. While it is shown in [Zreda et al., 2012] that the chemical composition becomes irrelevant as soon as even a small quantity of water is added.

## 2.2 Electrical resistivity tomography

Electrical Resistivity Tomography (ERT) is a geophysical method employed to determine the spatial distribution of the bulk electrical conductivity  $\sigma$  [ $\text{Sm}^{-1}$ ], or its inverse, the bulk electrical resistivity  $\rho$  [ $\Omega\text{m}$ ], of the subsurface.

An electric current is injected into the ground through a pair of current electrodes (C1, C2) also commonly called (A, B), and the resulting electric potential field is measured by a second pair of potential electrodes (P1, P2) or (M,N). The measured potential differences contain information about the electrical properties of the subsurface, as these influence the flow paths of electric current and, consequently, the shape of the electric field. Similarly to Fermat's principle in optics, which states that light always travels through the path that minimizes travel time, the electric current preferentially flows along paths showing minimal resistance.

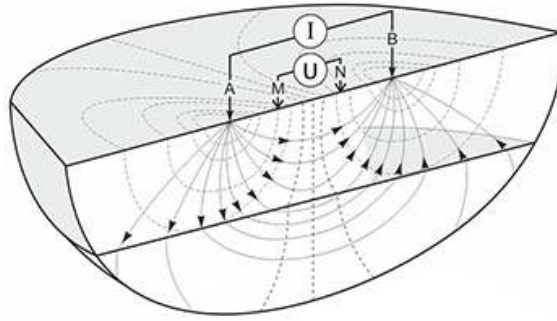


Figure 2.6: Schematic representation of current and potential electrode in ERT technique.

To describe the behavior of the electric potential field, it is useful to begin with the *microscopic form of Ohm's law*:

$$\mathbf{J} = \sigma \mathbf{E} \quad (2.5)$$

where  $\mathbf{E}$  is the electric field,  $\mathbf{J}$  is the current density vector, and  $\sigma$  is the electrical conductivity. Given that electrostatic fields are conservative, the electric field can be expressed as the negative gradient of the electric potential:

$$\mathbf{E} = -\nabla V \quad (2.6)$$

Substitution into equation 2.5 yields:

$$\mathbf{J} = -\sigma \nabla V \quad (2.7)$$

In direct current (DC) conditions, the principle of conservation of electric charge applies, leading to:

$$\nabla \cdot \mathbf{J} = 0 \quad (2.8)$$

This results in the governing equation for the electric potential in a medium with spatially variable and potentially anisotropic conductivity:

$$\frac{\partial}{\partial x} \left( \sigma_x(x, y, z) \frac{\partial V}{\partial x} \right) + \frac{\partial}{\partial y} \left( \sigma_y(x, y, z) \frac{\partial V}{\partial y} \right) + \frac{\partial}{\partial z} \left( \sigma_z(x, y, z) \frac{\partial V}{\partial z} \right) = 0 \quad (2.9)$$

In the case of a homogeneous and isotropic medium, equation 2.9 simplifies to the Laplace equation:

$$\nabla^2 V = 0 \quad (2.10)$$

As mentioned, current lines tend to concentrate in zones of lower resistivity. This behavior is governed by the *tangent law*. Considering a two-layer system with different resistivities  $\rho_1$  and  $\rho_2$ , separated by a horizontal interface, an incident current density  $\mathbf{J}_1$  impinges on the interface at an angle  $\theta_1$  and is refracted into  $\mathbf{J}_2$  at an angle  $\theta_2$ .

In electrostatics, the absence of magnetic fields implies  $\nabla \times \mathbf{E} = 0$ , which leads to the continuity of the tangential component of the electric field:

$$E_{x1} = E_{x2} \quad \Rightarrow \quad J_{x1}\rho_1 = J_{x2}\rho_2 \quad (2.11)$$

Additionally, the continuity of current across the interface requires:

$$J_{z1} = J_{z2} \quad (2.12)$$

Combining these conditions yields the tangent law:

$$\frac{J_{x1}}{J_{z1}}\rho_1 = \frac{J_{x2}}{J_{z2}}\rho_2 \quad \Rightarrow \quad \frac{\tan \theta_1}{\tan \theta_2} = \frac{\rho_1}{\rho_2} \quad (2.13)$$

This implies that when  $\rho_1 < \rho_2$ , then  $\theta_1 < \theta_2$ .

### 2.2.1 Principles

In practice, the subsurface resistivity distribution is inferred through a sequence of measurements involving different configurations of current and potential electrode

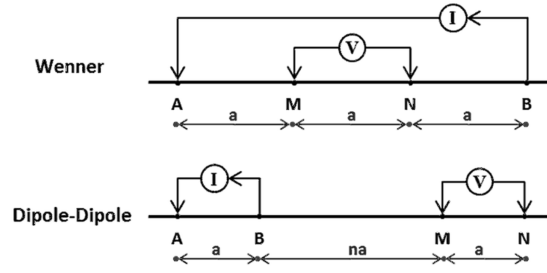


Figure 2.7: Top: Wenner electrode configuration. Bottom: dipole-dipole configuration

pairs. These measurements yield a dataset of transfer resistances, which encode information about the spatial variability of the subsurface’s electrical properties. Electrodes are typically deployed along linear profiles or two-dimensional grids at the ground surface, with the specific array geometry and measurement protocol tailored to the investigation objectives.

For example, to enhance sensitivity to deeper structures, measurement sequences may emphasize configurations such as the Wenner array (Figure 2.7, which exhibit relatively greater depth sensitivity. Conversely, if higher resolution in the shallow subsurface is required, dipole–dipole configurations may be preferred due to their lateral resolution characteristics. A commonly adopted empirical rule indicates that the maximum depth of investigation achievable is approximately one-fifth of the total electrode spread length.

Departures of the observed transfer resistances from those predicted under the assumption of a homogeneous half-space reflect the presence of subsurface heterogeneities. Recovering the spatial distribution of electrical resistivity  $\rho$ , from these data requires the solution of an inverse problem governed by Poisson’s equation, typically formulated and solved using regularized nonlinear inversion techniques.

The inversion process consists of minimizing an objective function  $\psi(\mathbf{m})$  that, due to the ill-posed nature of the problem leading to non-uniqueness of the solution [Vanderborght et al., 2013], can be expressed as a weighted sum of the data misfit and a regularization term:

$$\psi(\mathbf{m}) = \psi_d(\mathbf{m}) + \alpha\psi_m(\mathbf{m}) \quad (2.14)$$

with  $\psi_d(\mathbf{m})$  being the data misfit designed as

$$\psi_d(\mathbf{m}) = \|\mathbf{W}[\mathbf{d} - \mathbf{f}(\mathbf{m})]\| \quad (2.15)$$

where  $\mathbf{m}$  is the vector of unknowns (electrical resistivity for each discretization grid cell);  $\mathbf{d}$  is the vector of data (resistances measured with each quadrupole);  $\mathbf{f}(\mathbf{m})$  is the vector of electrical resistances predicted by the forward model derived from the numerical solution of eq. 2.9;  $\mathbf{W}$  is a data weighting matrix associated with the individual data errors. And  $\psi_{\mathbf{m}}(\mathbf{m})$  is a regularization term taking smaller values for smoother  $\mathbf{m}$  fields; and  $\alpha$  is a regularization parameter that controls the trade-off between  $\psi_{\mathbf{d}}$  and  $\psi_{\mathbf{m}}$  [Camporese et al., 2015].

In cases where no detailed prior information is available about the resistivity distribution, regularization is often implemented by promoting smoothness in the model. This approach favors the smoothest resistivity distribution that still adequately explains the observed data, following *Occam's principle* [Constable et al., 1987]. According to this principle, among all possible models that explain the observations, the simplest, or least complex, model is preferred. In the context of ERT inversion, this translates into penalizing sharp resistivity contrasts unless strongly supported by the data, thereby yielding a stable and geologically plausible solution.

## 2.3 Frequency domain electromagnetic induction method

Frequency domain electromagnetic (FDEM) methods belong to the broader class of geophysical techniques that exploit the behavior of electromagnetic (EM) fields. For this reason, it is appropriate to recall the macroscopic Maxwell equations, which describe the fundamental dynamics of electric and magnetic fields in matter:

$$\nabla \times \mathbf{E} = -\frac{\partial \mathbf{B}}{\partial t} \quad (2.16)$$

$$\nabla \cdot \mathbf{D} = 0 \quad (2.17)$$

$$\nabla \times \mathbf{H} = \mathbf{J} + \frac{\partial \mathbf{D}}{\partial t} \quad (2.18)$$

$$\nabla \cdot \mathbf{B} = 0 \quad (2.19)$$

By combining these equations, one can derive the wave equations for the electric and magnetic fields in a homogeneous, isotropic, linear, and source-free medium:

$$\nabla^2 \mathbf{E} - \sigma \mu \frac{\partial \mathbf{E}}{\partial t} = \epsilon \mu \frac{\partial^2 \mathbf{E}}{\partial t^2} \quad (2.20)$$

$$\nabla^2 \mathbf{H} - \sigma \mu \frac{\partial \mathbf{H}}{\partial t} = \epsilon \mu \frac{\partial^2 \mathbf{H}}{\partial t^2} \quad (2.21)$$

Here,  $\sigma$  denotes the electrical conductivity,  $\epsilon$  the dielectric permittivity, and  $\mu$  the magnetic permeability of the medium. The right-hand side (RHS) of each equation represents wave propagation, while the first-order time derivative on the left-hand side (LHS) accounts for energy dissipation.

To better understand the operative regime of FDEM systems, it is convenient to transform these equations into the frequency domain via a Fourier transform. Taking the electric field as an example, the time-domain wave equation becomes:

$$\nabla^2 \mathbf{E} - i\mu\omega\sigma\mathbf{E} = -\mu\epsilon\omega^2\mathbf{E} \quad (2.22)$$

By comparing the magnitudes of the attenuation and propagation terms, we define the *loss factor* P:

$$P = \frac{\mu\omega\sigma}{\mu\epsilon\omega^2} = \frac{\sigma}{\epsilon\omega} \quad (2.23)$$

Two distinct regimes can be identified based on the value of  $P$ : When  $P \gg 1$  (i.e., high conductivity and/or low frequency), the attenuation term dominates. The fields behave diffusively, and electromagnetic induction (EMI) methods are applicable. Conversely, when  $P \ll 1$  (i.e., low conductivity and/or high frequency), the wave propagation term dominates. In this regime, EM wave methods such as ground-penetrating radar (GPR) are more appropriate.

Electromagnetic induction techniques typically operate in the frequency range 0.1 kHz – 1 MHz, while radar techniques use much higher frequencies, between 100 MHz – 1 GHz.

EMI methods are further subdivided into frequency domain and transient (time domain) techniques. In this work, we focus exclusively on frequency domain EMI methods, particularly under near-field conditions.

### 2.3.1 Principles

FDEM instruments operate by generating a time-varying primary magnetic field via a transmitting coil. According to Faraday’s law, this changing field induces eddy currents in the subsurface, which in turn generate a secondary magnetic field as described by the Ampère-Maxwell law. This secondary field is sensed by a receiver coil, and, due to Faraday’s law, the magnetic flux through the receiver coil induces a voltage, which is the measured signal.

The phase difference between the primary and secondary fields reflects the electrical and magnetic properties of the subsurface. As illustrated in Figure 2.8, the secondary magnetic field lags behind the primary field by a phase angle  $\Theta = \frac{\pi}{2} + \phi$ , where:

$$\phi = \tan^{-1}(\omega\mu_0\sigma s^2) \quad (2.24)$$

and the fields can be expressed as:

$$H_p = H_{p0} e^{i\phi_0} \quad (2.25)$$

$$H_s = H_{s0} e^{i(\frac{\pi}{2} + \phi)} \quad (2.26)$$

The total measured signal can be decomposed into two components: the *in-phase*

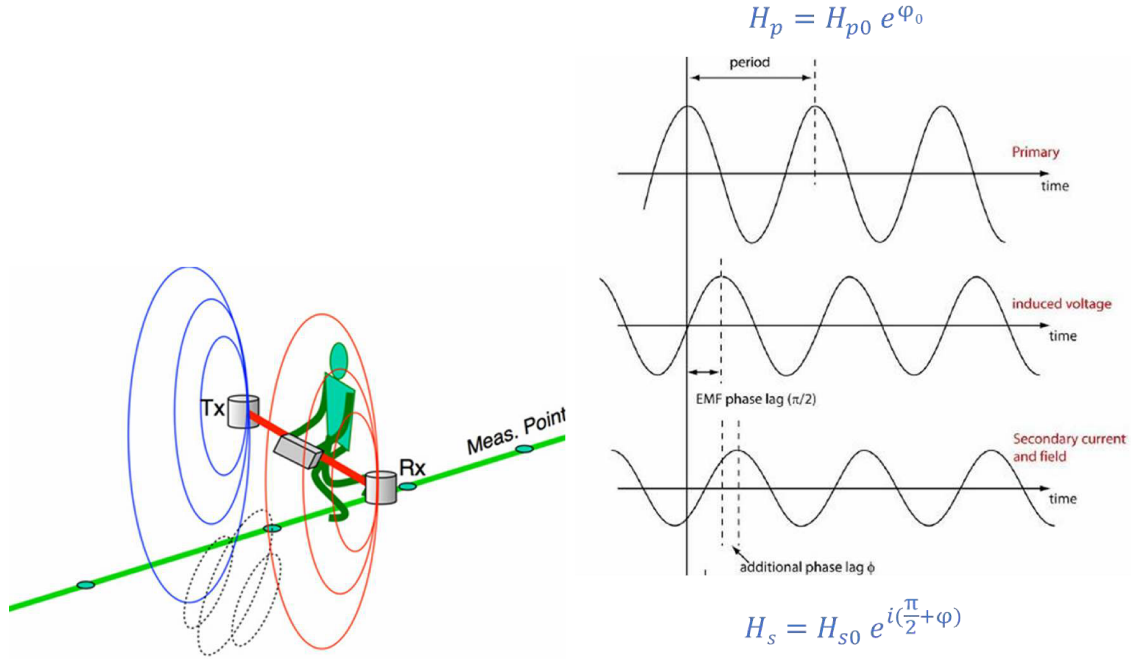


Figure 2.8: Left: schematic of transmitter-receiver configuration. Right: primary and secondary magnetic fields with phase shift.

component, primarily sensitive to magnetic permeability  $\mu$  and the *quadrature* (*out-of-phase*) component, primarily sensitive to electrical conductivity  $\sigma$ . To quantitatively interpret the measurements, the ratio of secondary to primary field amplitudes is studied using the response function  $f(\alpha)$ , which depends on the *induction number*  $\alpha$ :

$$\left( \frac{H_s}{H_p} \right)_{h/v} = f(\alpha) \quad , \quad \alpha = \frac{s}{\delta} = s \sqrt{\frac{\omega \mu_0 \sigma}{2}} \quad (2.27)$$

where:

- $s$  is the intercoil spacing (see Figure 2.8, left),
- $\delta$  is the skin depth,
- $\omega = 2\pi f$  is the angular frequency,
- $f$  is the signal frequency,
- $\mu_0$  is the magnetic permeability of free space (assuming  $\mu \approx \mu_0$ ),
- $\sigma$  is the electrical conductivity of the medium.

In general, the response functions for vertical and horizontal coil orientations are complex and nonlinear with respect to  $\alpha$  McNeill, 1980. However, when  $\alpha \ll 1$ , the so-called *low induction number (LIN)* regime, the response simplifies to:

$$\left(\frac{H_s}{H_p}\right)_h \simeq \left(\frac{H_s}{H_p}\right)_v \simeq \frac{i\alpha^2}{2} = \frac{i\omega\mu_0\sigma s^2}{4} \quad (2.28)$$

Achieving  $\alpha \ll 1$  requires the coil spacing  $s$  to be much smaller than the skin depth  $\delta$ , or equivalently:

$$\omega \ll \frac{2}{\mu_0\sigma s^2} \quad (2.29)$$

Once a coil spacing  $s$  is chosen and the expected maximum subsurface conductivity is estimated, the operating frequency is selected to satisfy this condition and remain within the LIN approximation. Under this assumption, the secondary field is linearly proportional to the ground conductivity, and exhibits a phase lead of  $90^\circ$  relative to the primary field (assuming non-magnetic ground, i.e.,  $\mu = \mu_0$ ) and from the quadrature component of the measured signal, one can derive the *apparent conductivity*  $\sigma_a$  as:

$$\sigma_a = \frac{4}{\mu_0\omega s^2} \cdot \frac{H_{sQ}}{H_{pQ}} \quad (2.30)$$

where the subscript Q denotes the quadrature component.

In practice, FDEM instruments acquire multiple measurements over the same location using either different coil spacings (geometric sounding) or different operating frequencies (frequency sounding). This strategy enables depth sensitivity and allows for inversion procedures to recover 1D conductivity profiles.

As with electrical resistivity tomography (ERT), inversion algorithms are used to construct subsurface models. However, unlike ERT, which provides a true 2D model, FDEM typically yields a pseudo-2D result, which consists of interpolated 1D profiles.



# Chapter 3

## Material and Methods

### 3.1 Study Site: Geology, Geomorphology and Vegetation

The study site is located in Borgo Grignanello, within the municipality of Castellina in Chianti (Siena province), in the heart of the Chianti Classico wine region. The surrounding land use is dominated by vineyards and olive groves, while approximately 62% of the territory is classified as forest according to [Masnaghetti, 2022]. The area is predominantly hilly, with elevations ranging from 300 to 500 m above sea level, and locally reaching up to about 900 m in the highest sectors.



Figure 3.1: Site location in Italy.

From a geological perspective, the site lies within the *External Ligurian Domain*. Two formations are present in the vicinity of the study area (Figure 3.2). The study site itself is located on the **Sillano–Santa Fiora Formation**. In this area, the

formation is composed mainly of gray to brown clays and calcilitites.

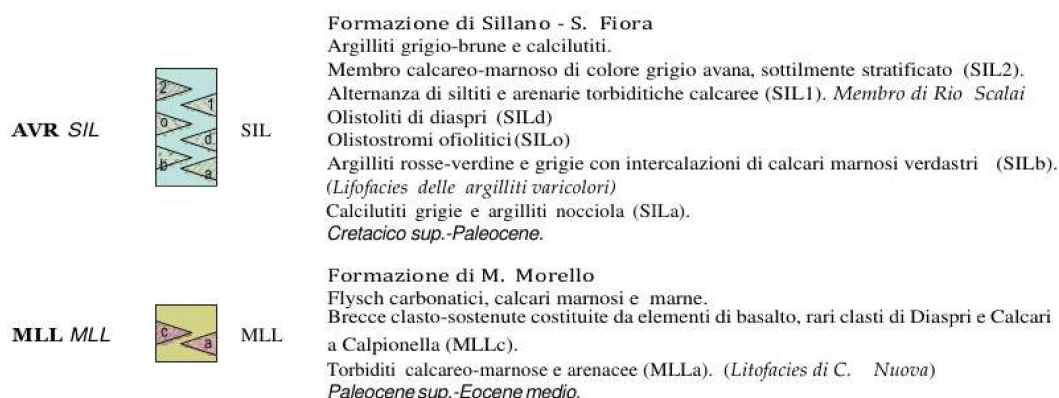
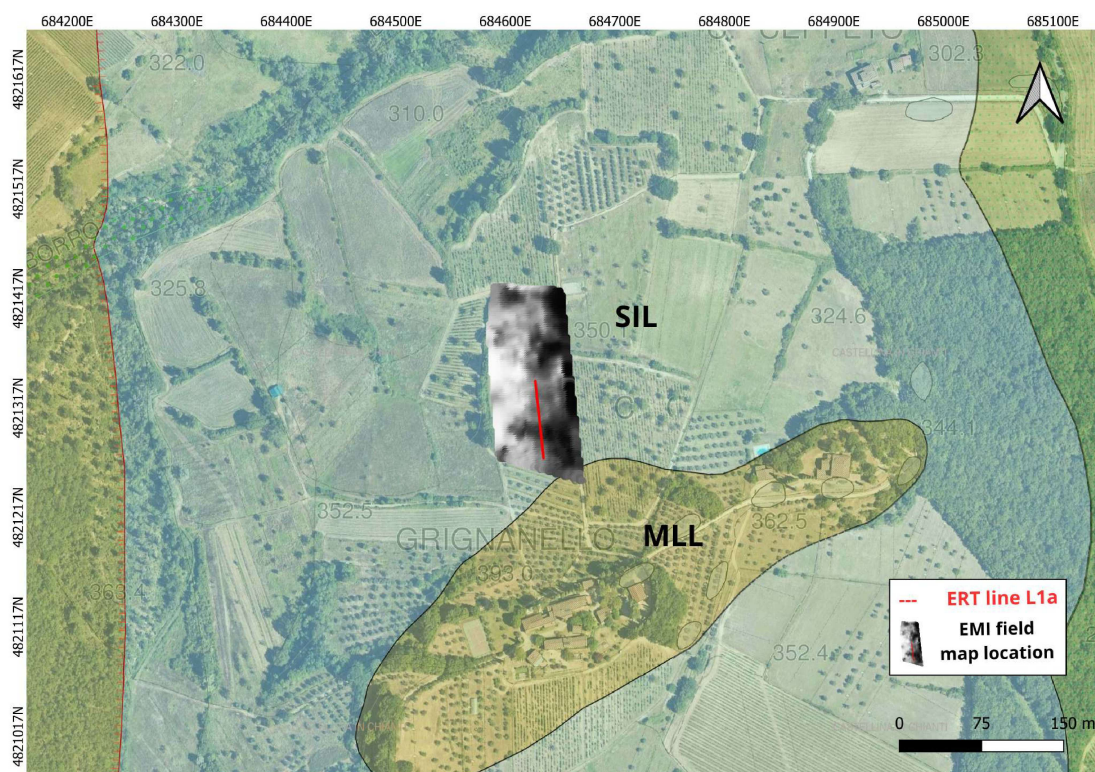


Figure 3.2: Area of the study site around Grignanello showing the regional geological map in 1:10.000 scale. To help the orientation, the site where the majority of the measurements were performed is covered by the greyscale map of the EMI data, and the central ERT line (L1a), which is 72m long, is also drawn in red.

The lithology is expressed in its typical facies, assigned to the Upper Cretaceous–Paleocene [Regione-Toscana, 2007]. Immediately below the village buildings, the substrate changes to the **Monte Morello Formation** (also assigned to the External Ligurian Domain). This unit is characterized by carbonatic flysch, consisting of alternating marly limestones and marls, and has been dated to the Upper Paleocene–Middle Eocene. The juxtaposition of these two formations reflects the

complex tectono-stratigraphic setting of the Chianti sector of the Northern Apennines.

Pedological information provided by Regione Toscana indicates that soils in the Castellina in Chianti area are typically deep, only slightly gravelly, and dominated by silty clay to clay loam textures. They are strongly calcareous, weakly to moderately alkaline, and moderately well-drained. Such properties influence both infiltration capacity and water retention, with implications for hydrogeophysical surveys. The CRNP sensor is installed within an active vineyard characterized by old vines approximately 1.5–2 m in height, consistent with traditional Chianti cultivation systems. The plants are supported by concrete poles spaced every few plants, a technique typical of older viticultural practices. During both measurement campaigns, the vineyard soil was not recently tilled, and inter-row spaces were covered by grass. Importantly, no chemical treatments were applied immediately before or during the survey periods, ensuring that vegetation and soil moisture conditions remained undisturbed by agricultural practices.

The local topography is characterized by the alternation of gentle slopes with steeper sections. At the study site, the land surface dips toward the north, with a marked change in slope occurring approximately 20 m downslope of the CRNP installation. This geometry favors surface runoff, although not at critical levels. The slope configuration is not expected to exert a significant influence on cosmic-ray neutron propagation or on the spatial footprint of the CRNP measurements, yet it must be considered in hydrological interpretation.

Together with the described geology, pedology, and vegetation heterogeneity, this gentle but variable morphology influences the spatiotemporal dynamics of runoff and infiltration. The resulting hydrological complexity remains elusive and yet fundamental for the region's agroforestry system.

## 3.2 Geophysical Data Acquisition and Processing

The geophysical survey was carried out to assess the heterogeneity of the site, particularly in terms of ground conductivity distribution, which can help infer variations in lithology and moisture content. For this purpose, methods commonly employed in hydrogeophysical investigations, namely ERT and FDEM, were used, as previously introduced. The surveys were essential to support and enhance the interpretation of the CRNS time series. Another key activity, fundamental for calibrating CRNS count conversions, was the direct measurement of volumetric water content (VWC) and bulk density, possible through the collection of 13 soil samples.

Figure 3.3 illustrates the spatial layout of the ERT lines and soil sample locations, along with the positions of the CRNP.

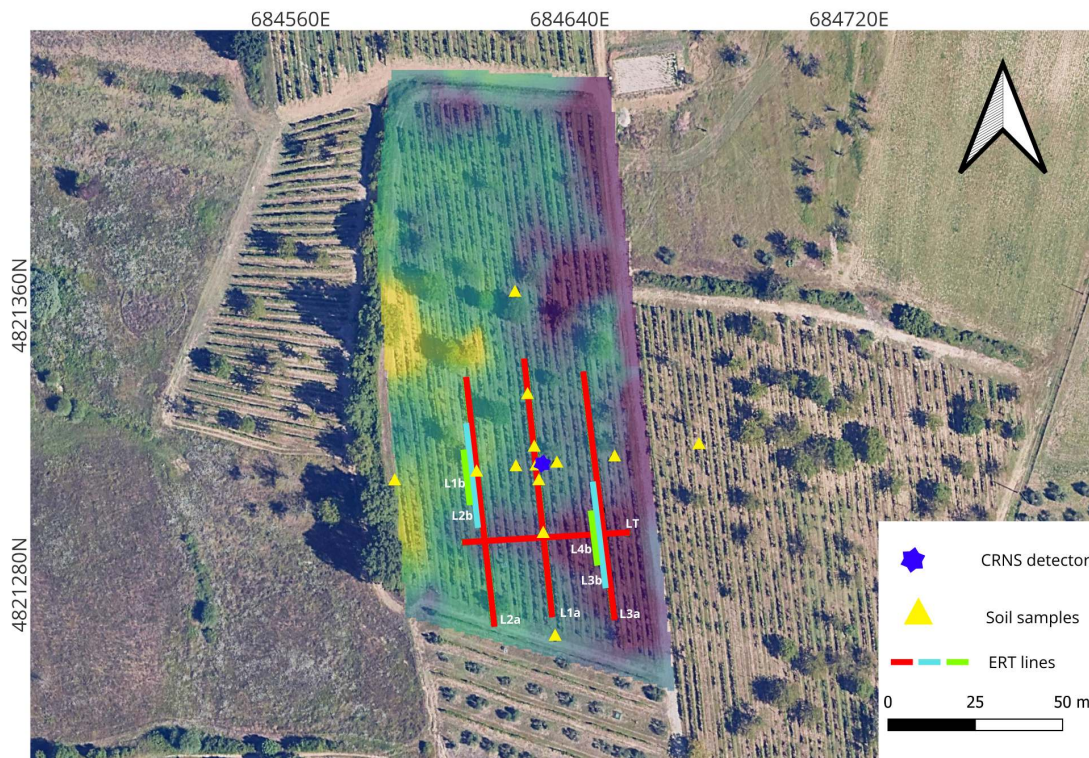


Figure 3.3: Survey map showing the eight ERT lines from both campaigns, sample locations, and the CRNP position. In the background, the conductivity map obtained with the EMI inversion, corresponding to  $\sim 1.25$  m (bgl).

These were strategically distributed in a cross pattern within a 50 m radius from the detector. The resulting VWC and bulk density values were also critical inputs

for the numerical simulations described in the following section.

Preliminary insights into the subsurface heterogeneity of the vineyard were already available from earlier ERT campaigns, which informed the planning of new ERT lines. Moreover, the spatial sensitivity of the CRNP (see Section 2.1.3) guided the sample distribution [M. Köhli et al., 2015].

The first survey was conducted between November 14 and 15, 2024, which firstly involved the acquisition of four ERT lines and of the FDEM mapping. On the second day, sampling activities were completed alongside the remaining FDEM measurements.

A second campaign followed between March 25 and 26, 2025. This phase aimed to acquire high-resolution ERT data, using electrode spacings of 20 cm and 40 cm, and to characterize an adjacent vineyard to the east, in order to investigate lithological continuity across the site. Additionally, the CRNP was connected to a server to enable remote data monitoring. TDR mapping was also performed, but its results will be analyzed in future work.

### 3.2.1 Samples: Acquisition, Analysis, and Results

The sample collection strategy was designed based on the CRNP’s sensitivity footprint, which is significantly higher in the immediate vicinity of the detector and decreases with distance. For this reason, samples were collected in a cross-shaped layout centered on the CRNP. One direction followed the vineyard rows (aligned approximately North–South), while the other was perpendicular, crossing multiple plant rows (see Figure 3.3).

The first sampling point was positioned at  $\approx 0$  m from the detector along the North–South axis, approximately 1 m from the nearest plant row. Additional sampling locations were distributed at distances of [5 20 20 50] m in both directions, resulting in a total of 13 distinct sampling locations.

To investigate possible vertical variability in soil properties, two samples were collected at each location from different depths: one from 0 to  $\sim 15$  cm, and the other

from 15 to  $\sim 25$  cm depth (as deep as field conditions allowed).

A manual core drill was used for sample extraction and GPS coordinates were recorded at each location (see Figure 3.4).

The coordinates of the sampling points and the CRNP are listed in Table 3.1.



Figure 3.4: Core sampling using a manual core drill (left); sample hole in the field (right).

All samples were weighed in the field using a balance with a resolution of 1 g and then oven dried in the laboratory at 50°C. The drying process was monitored by weighing the samples at regular intervals until their mass stabilized.

The volume of the sample was estimated by measuring the depth of each hole in the field and using the known diameter of the core drill. Given field limitations, a rigorous volume estimation was not possible. Therefore, uncertainty was approximated by measuring the deepest and shallowest points within each hole and taking the semidifference as the error estimate of the height.

The bulk density and the VWC were calculated using equations 3.1 and errors were propagated accordingly.

$$\rho_b = \frac{m_{\text{dry}}}{V_{\text{tot}}} \quad , \quad \text{VWC} = \frac{\rho_b}{\rho_w} \frac{m_0 - m_{\text{dry}}}{m_{\text{dry}}} \cdot 100 \quad (3.1)$$

where  $\rho_b$  is the bulk density,  $m_{\text{dry}}$  is the mass after complete drying,  $V_{\text{tot}}$  is the total extracted volume,  $m_0$  is the field measured mass and  $\rho_w$  is the density of water, assumed to be  $1 \text{ g/cm}^3$ .

The results, including sample coordinates, bulk density, and VWC, are reported in Table 3.1.

The average bulk density across all samples was  $0.89 \pm 0.20 \text{ g/cm}^3$ . When separating shallow and deep samples, the average values were  $0.82 \pm 0.08 \text{ g/cm}^3$  and  $0.96 \pm 0.26 \text{ g/cm}^3$ , respectively, indicating no significant vertical gradient in density within the first 25 cm. Similarly, the overall VWC was  $20.1 \pm 4.5 \%$ . When disaggregated, shallow samples averaged  $19.1 \pm 3.1 \%$ , while deeper samples averaged  $20.1 \pm 5.4 \%$ . Moreover, neither bulk density nor VWC exhibited a discernible spatial pattern. These observations can be speculated observing Table 3.1 and Figure 3.5. This suggests a relatively homogeneous superficial soil layer. TDR mapping, addressed in future work, will help confirm whether the upper layer exhibits consistent behavior or is influenced by deeper heterogeneities.

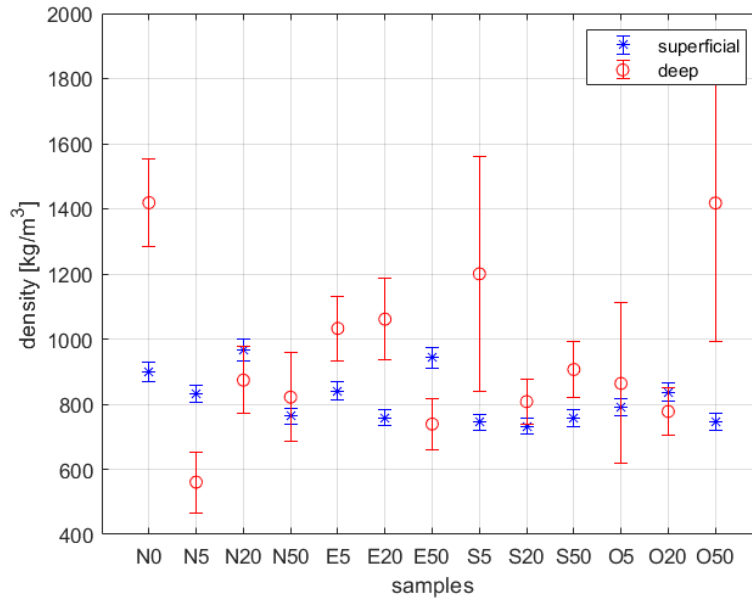


Figure 3.5: Bulk density values from shallow and deep samples. No evidence of a density gradient or spatial pattern is observed.

The relatively low average bulk density, which was lower than initially expected, warranted further investigation. One possible cause is the high organic matter content,

Sample label	$\rho_b$ [kg/m <sup>3</sup> ]	VWC [%]	x	y	z
N1	900.6	21.9	43.52150087	11.28462214	361.025
N2	1418.7	33.2	43.52150087	11.28462214	361.025
N3	831.9	21.9	43.52176756	11.28459011	358.35
N4	560.5	12.8	43.52176756	11.28459011	358.35
N5	966.6	23.2	43.52190151	11.28457841	357.096
N6	873.9	21.0	43.52190151	11.28457841	357.096
N7	762.8	21.0	43.52194438	11.28457001	356.768
N8	821.6	22.8	43.52194438	11.28457001	356.768
S1	840.6	22.0	43.52198977	11.2845642	356.384
S2	1032.6	20.4	43.52198977	11.2845642	356.384
S3	758.5	17.2	43.52212529	11.28454806	354.694
S4	1061.1	22.1	43.52212529	11.28454806	354.694
S5	943.2	20.0	43.52239072	11.28451677	350.128
S6	739.0	13.3	43.52239072	11.28451677	350.128
E1	745.1	15.1	43.52191504	11.28406903	353.395
E2	1200.3	27.4	43.52191504	11.28406903	353.395
E3	731.9	19.3	43.52193468	11.28436082	355.737
E4	807.9	21.4	43.52193468	11.28436082	355.737
E5	756.8	17.9	43.52194385	11.28450036	356.466
E6	906.4	21.5	43.52194385	11.28450036	356.466
O1	791.1	20.5	43.52194965	11.28464182	357.05
O2	863.8	20.2	43.52194965	11.28464182	357.05
O3	836.4	14.2	43.52196176	11.28485066	357.571
O4	777.5	15.9	43.52196176	11.28485066	357.571
O5	746.2	14.2	43.52198511	11.28515246	357.632
O6	1417.7	22.9	43.52198511	11.28515246	357.632

Table 3.1: Samples location in plane coordinates. First line shows the cosmic ray neutron probe position while the labels in the first columns were used to name the sample according to direction (N-North, S-south and so on) with respect to the detector position and the number is just sequential, considering that for every location two soil samples were collected odd numbers are for shallow samples and even for deep. Bulk density values in kg/m<sup>3</sup> and VWC in percentage for all 13 samples.

Sample	LOI 450°C [%]
E2	9.85
E3	9.99
O2	8.43
O5	7.58
O1	9.42
O6	8.52

Table 3.2: Mass loss percentages from LOI analysis at 450°C, used to estimate organic matter content in selected samples.

which is known to reduce the bulk density. Therefore, six samples (both shallow and deep) were analyzed using the loss-on-ignition (LOI) method at 450° C to estimate the organic matter content. The results are shown in Table 3.2.

### 3.2.2 ERT Survey: Acquisition, Processing, and Results

To investigate subsurface heterogeneity around the CRNP and confirm previous interpretations, several ERT lines were acquired during both field campaigns. The surveys were carried out using a Syscal Terra resistivity meter (Iris Instruments) with 96 electrode connections.

During the first campaign, three parallel profiles ( $L1a$ ,  $L2a$ , and  $L3a$ ) were laid along the north-south direction, following the vineyard rows (see Figure 3.3). Each line consisted of 48 electrodes spaced 1 meter apart, with one roll-along section, yielding profiles approximately 72 meters



Figure 3.6: Site location in Italy.

in length. An additional transverse line ( $LT$ ) was acquired in the east-west direction, perpendicular to the vineyard rows, with a total length of 48 meters and a 1-meter electrode spacing. This line was designed to investigate a known lithological boundary inferred from earlier measurements. All ERT lines used dipole–dipole electrode configurations with multiple skips to increase lateral resolution and depth coverage.

During the second campaign (March 2025), four additional lines ( $L1b$ ,  $L2b$ ,  $L3b$ , and  $L4b$ ) were acquired to improve near-surface resolution. For these lines, a shorter electrode spacing of 20 cm and 40 cm was used. These lines partially overlapped with previous profiles  $L2a$  and  $L3a$  to allow comparison and continuity checks. This high-resolution acquisition aimed to better characterize the very shallow subsurface while still accounting for the importance of deeper features in groundwater dynamics. A summary of the lines configuration can be found in Table 3.3.

The collected data exhibited excellent quality, with contact resistances of only a few  $k\Omega$  and reciprocal errors generally within 2.5%. A representative example of the

Line Name	Tot. Length [m]	Electrode Spacing [m]	Direction	Relative Position to L1a
L1a	72	1	S-N	Central (reference line)
L2a	72	1	S-N	West of L1a
L3a	72	1	S-N	East of L1a
LT	48	1	W-E	Crosses L1a L2a L3a
L1b	28.4	0.40	S-N	Overlapping L2a
L2b	14.2	0.20	S-N	Overlapping L2a
L3b	28.4	0.40	S-N	Overlapping L3a
L4b	14.2	0.20	S-N	Overlapping L3a

Table 3.3: Summary of the ERT lines performed during both field campaigns. The table provides line name, length, electrode spacing, number of roll-on segments, acquisition direction, and relative position with respect to line L1a, which is the central S–N profile located near the CRNP.

reciprocal error distribution is shown in Figure 3.7.

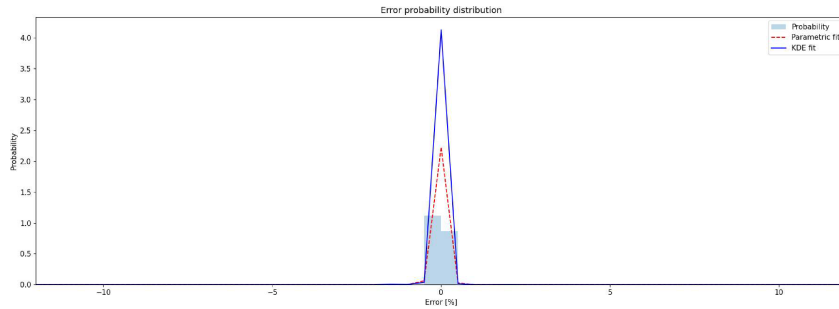


Figure 3.7: Representative distribution of reciprocal errors from ERT data. Reciprocal errors were generally below 2.5%.

Processing and inversion were performed using ResIPy [Blanchy et al., 2020], a Python-based interface built on the R\* codes developed by Andrew Binley. In all cases, filtering based on reciprocal errors was applied. Given the high quality of the data, measurements with error  $> 2.5\%$  were removed, and in the worst scenario only 26 points were excluded. A linear error model was fitted to find the regularization parameters for the inversion, which in all cases converged in a few iterations, with a final RMS misfit of 1.00.

The inversion results in terms of the conductivity sections are shown in Figure 3.8 that reveal clear lateral and vertical heterogeneities in the shallow lithology. This is consistent with the expected soil layering and structural variation.

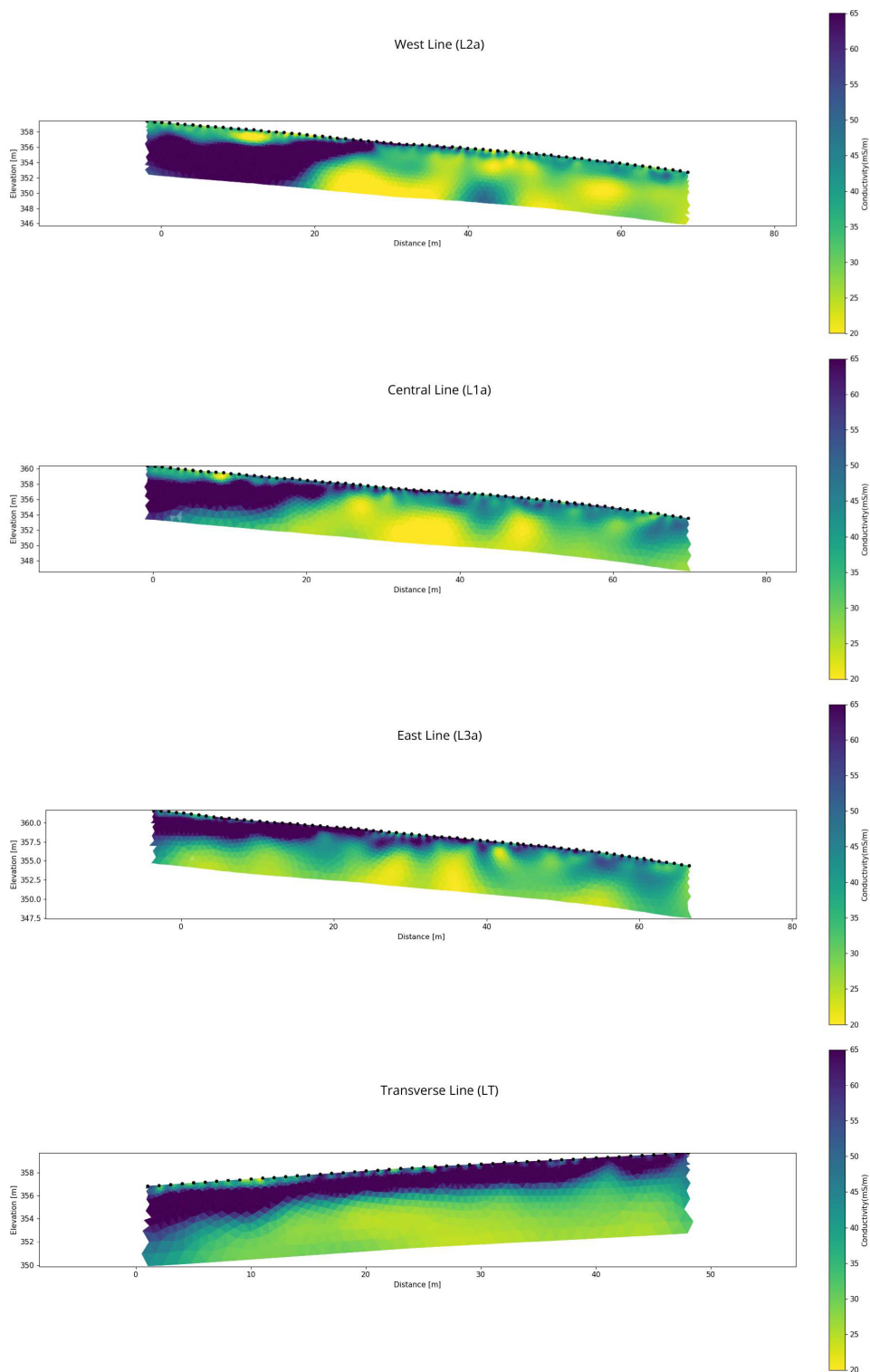


Figure 3.8: (Starting from the top) Inversion results from profiles *L2a*, *L1a*, *L3a*, and *LT* processed using ResIPy. Filtered applied on reciprocal errors at 2.5%, and linear error model to find the regularization parameters

### 3.2.3 FDEM Survey: Acquisition, Processing, and Results



Figure 3.9: *Mini Explorer* by *GF Instruments*. Multi-coil system for the frequency domain electromagnetic method acquisition. Automatic sampling with active GPS recording was performed by covering the whole field.

The FDEM survey was performed using the CMD Mini Explorer conductivimeter (GF Instruments). This instrument includes three transmitter–receiver coil spacings: 0.32 m, 0.71 m, and 1.18 m, for a total of 4 coils in the system, and supports both vertical and horizontal coplanar configurations. This enables the exploration of different depth ranges and the acquisition of apparent conductivity data characterized by different sensitivity functions.

Field data were collected walking along parallel transects between all vineyard rows. Choosing an automatic sampling frequency of 2 Hz with GPS recording (with precision of  $\pm 1$  m) allowed us to create a map of the part of the footprint close to the CRNP. The measurement grid ensured coverage of the vineyard where the CRNP is located.

A pseudo-2D conductivity section was obtained by inverting the multicoil FDEM data using the EmagPy software package [McLachlan et al., 2021]. To enhance consistency with ERT-derived subsurface properties, the FDEM conductivity values were calibrated using obtained resistivity models from the *L3b* ERT line (with

40 cm electrode spacing). Specifically, a linear correlation was identified between the ERT-derived conductivities and the raw FDEM data, which was then applied as a calibration factor across the entire FDEM dataset.

The final conductivity maps were obtained via spatial interpolation using the Kriging algorithm implemented in QGIS. This allowed for the visualization of subsurface conductivity at multiple depth intervals across the field. Figure 3.10 presents the resulting conductivity maps at chosen depths: 0.25 m, 0.5 m, 0.75 m, 1.0 m, and 1.25 m.

### 3.2. GEOPHYSICAL DATA ACQUISITION AND PROCESSING

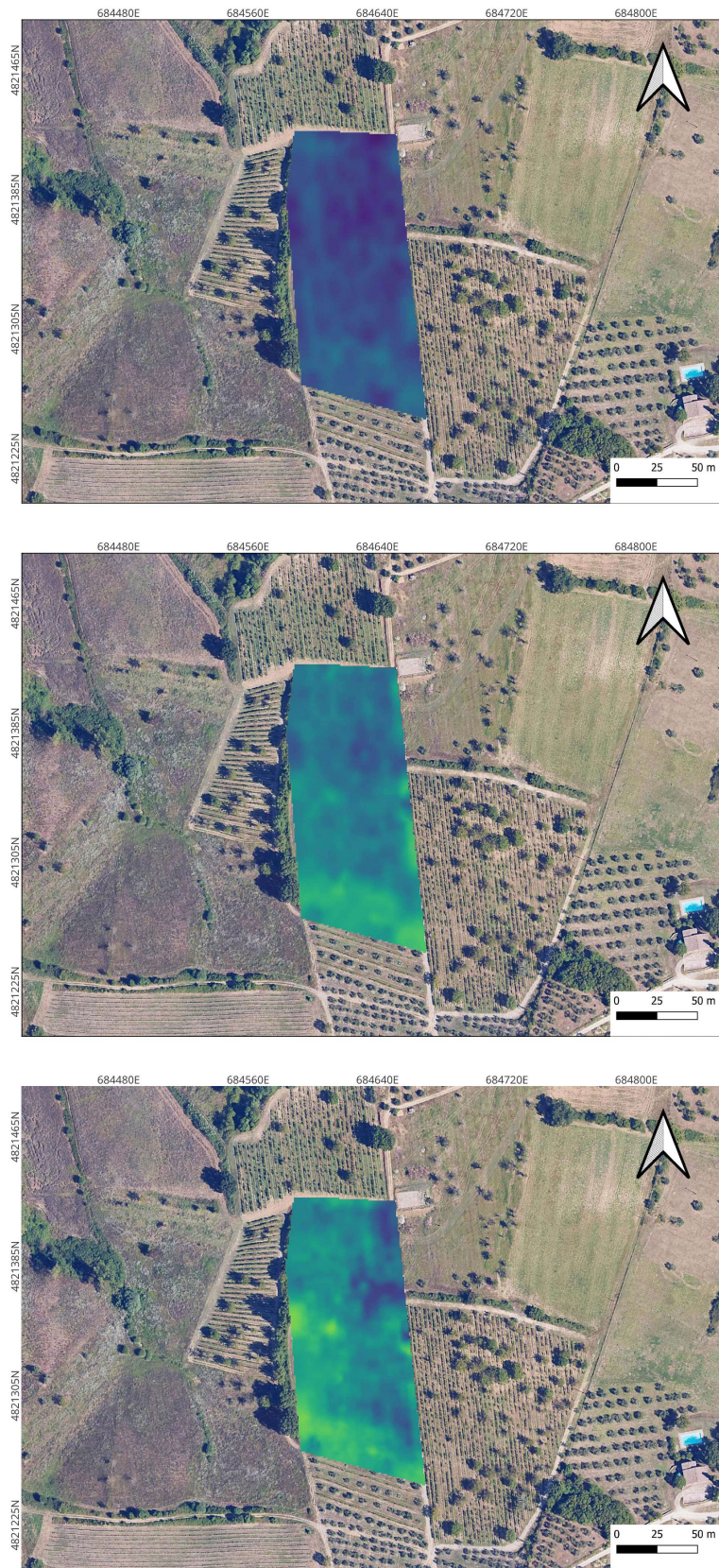


Figure 3.10: Interpolated FDEM conductivity maps at selected depths, respectively: 0.25 m, 0.5 m, and 0.75 m (continued in Figure 3.11).

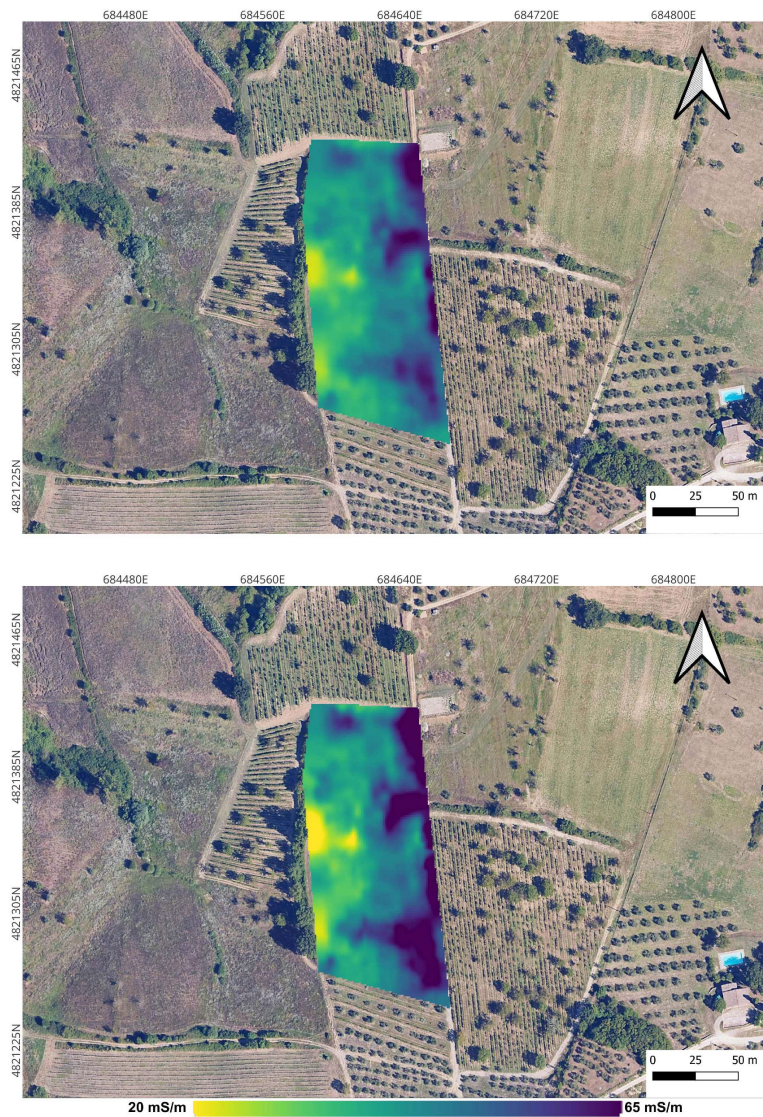


Figure 3.11: Interpolated FDEM conductivity maps at selected depths: 1.0 m and 1.25 m (continued from Figure 3.10).

### 3.3 Modeling and Monte Carlo simulations

The modeling of the environment and the simulation of neutron transport were essential to gain a deeper understanding of neutron behavior under varying environmental conditions and the corresponding detector response. Furthermore, these simulations enabled the study of the effects of site heterogeneities on the detector measurements, features that cannot be captured through field data alone, expanding the potential of CRNS technique.

Monte Carlo simulations are widely employed as an effective method for calculating neutron transport. The approach involves random sampling from predefined initial conditions. Specifically, particles are introduced at selected positions with defined energy and angular distributions, and their trajectories are then simulated probabilistically through the domain, based on relevant microscopic cross sections. In this manner, individual neutron tracks can be simulated and stored, allowing for the analysis of external influences on their paths. Moreover, neutron fluxes can be modeled with appropriate statistical accuracy, all while maintaining relatively low computational costs compared to alternative simulation tools [Weimar, 2022].

In the context of CRNS, the primary strength of a Monte Carlo transport code lies in its ability to realistically simulate how environmental conditions influence the neutron flux at the interface between the atmosphere and the land surface. These simulations provide the foundation for the derivation of analytical transfer functions, which describe the response of neutron flux to variations in environmental parameters, such as soil moisture.

#### 3.3.1 URANOS Monte Carlo Transport Code

The simulation tool used in this work is URANOS (Ultra Rapid Neutron-Only Simulation), a Monte Carlo-based code specifically developed for neutron transport in environmental contexts.

URANOS simulates elastic collisions across thermal, epithermal, and fast energy regimes, as well as inelastic scattering, neutron absorption, and absorption-like pro-

cesses such as evaporation<sup>1</sup>, which are particularly relevant for the elements encountered in environmental materials. The code is optimized by excluding unnecessary physical processes (e.g., fission, gamma cascades), resulting in significantly faster computational performance compared to general-purpose Monte Carlo codes.

URANOS employs a layered model architecture, where each layer is created by extruding a two-dimensional map into a voxel-based three-dimensional geometry. Each layer can either consist of a single homogeneous material or be subdivided into multiple regions using a two-dimensional matrix. Voxels are assigned predefined materials, each characterized by a specific isotope composition, atomic weight, and density. For example modeled pure air consists of 78%<sub>Vol</sub> Nitrogen, 21%<sub>Vol</sub> Oxygen and 1%<sub>Vol</sub> Argon, pressure at 1020 mbar; while the solid part in the soil is made of 75%<sub>Vol</sub> SiO<sub>2</sub> , 25%<sub>Vol</sub> Al<sub>2</sub>O<sub>3</sub> at a compound density of 2.86g/cm<sup>3</sup>.

The simulation domain typically includes three main layers: the neutron source, the detector (which may also be modeled as a virtual detector with finite spatial resolution rather than an infinite plane), and the ground. These layers can be further subdivided into sublayers with heterogeneous properties to reflect complex systems. Heterogeneities can be defined by importing tab-separated ASCII matrices with equal row and column dimensions or using grayscale PNG images. Integer or grayscale values are used to assign density, porosity, and material types to each voxel.

The parameters of the upper atmospheric layer, such as atmospheric depth and air humidity, can be freely customized.

URANOS adopts a distinctive approach in defining the cosmic neutron source. Unlike other studies, it provides a source specification tailored for the simulation of soil-moisture-dependent neutron transport which is near the atmosphere–soil interface. Depending on the scenario, particularly on atmospheric depth and humidity profiles, the simulated vertical extent can reach up to several kilometers.

The number of neutrons launched in the simulation is determined based on the de-

---

<sup>1</sup>Evaporation refers to the emission of fast neutrons following interactions of high-energy neutrons or protons with soil or air.

sired statistical accuracy. Increasing the number of particles improves the smoothness and reliability of the resulting data. A sample size on the order of  $10^7$  neutrons was suggested [M. Köhli et al., 2015] as well as found to be an effective compromise between computational effort and precision.

Neutron energies are sampled from a pre-calculated spectrum based on the work of [Sato and Niita, 2006]<sup>2</sup>. High-energy neutrons are emitted with a collimated angular distribution given by:

$$J(\alpha) = e^{-2.4(1-\cos(\alpha))} \quad (3.2)$$

where  $\alpha$  is the nadir angle.

URANOS is also peculiar because it uses the method of ray casting in order to keep track of the articles. This improves the accuracy in cases where only a specific subset of conditions will meet the criteria for scoring. Ray casting follows tracks from the source to the point of detection.

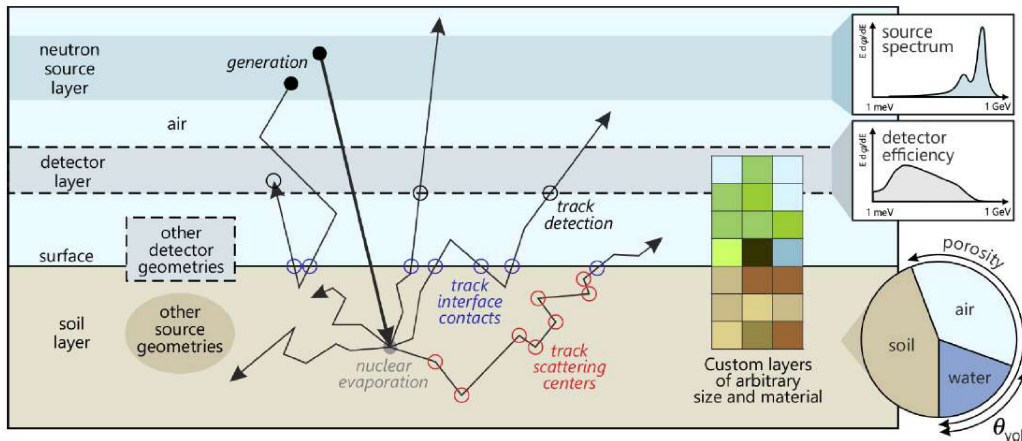


Figure 3.12: 2D Schematic (not to scale) of the 3D model setup and neutron transport processes. Neutrons are emitted from a source layer following an atmospheric energy spectrum, interact with soil via nuclear evaporation, and scatter through material layers before detection. The detector response depends on neutron energy, and environmental components are defined by adjustable material and density parameters.

<sup>2</sup>This study provides a reliable cosmic-ray neutron energy spectrum across various altitudes, geomagnetic cutoff rigidities, solar modulation conditions, and surface characteristics.

### 3.3.2 Modeling Site conditions

URANOS enables the user to simulate environmental conditions by specifying atmospheric composition and parameters (e.g., depth and humidity), location-specific values (such as geomagnetic cutoff rigidity), and ground composition. In this study, ground modeling played a central role, as most simulations involved variations in soil properties.

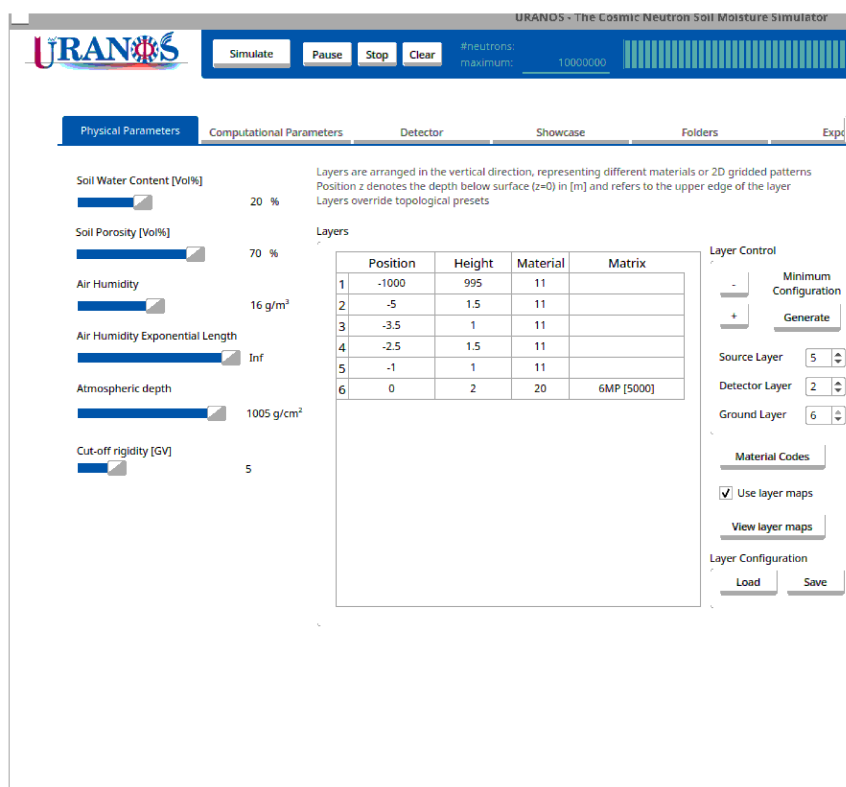


Figure 3.13: Parameter panel of URANOS GUI

To reproduce the specific conditions of the Borgo Grignanello site, the following parameters were defined: an air humidity of 16.0, g/m<sup>3</sup> (corresponding to 75% relative humidity at 25°C), atmospheric depth of 1013.0, g/cm<sup>2</sup>, and a geomagnetic cutoff rigidity of 5.0, GeV. A uniform humidity value was applied across all altitude layers, consistent with the software's standard configuration.

URANOS offers a set of predefined materials characterized by a defined chemical composition for environmental modeling. When simulating soil, various strategies can be adopted to better represent realistic scenarios beyond the default configuration (soil density of 2.86, g/cm<sup>3</sup> and 0% porosity). In this study, custom input

through PNG maps was employed to define spatial heterogeneities and enhance modeling flexibility.

Two key soil parameters were considered: bulk density and volumetric water content (VWC). While URANOS allows users to select default soil types with a specific VWC (ranging from 1% to 85%), a more precise modeling for the density was achieved by tuning porosity, density scaling factors, and water content to match known values from field samples. The relationship used to compute the actual density is given by:

$$\rho = f_d (\rho_{\text{def}} \cdot (1 - p) + \theta_{\text{cod}} \cdot \rho_w) \quad (3.3)$$

where  $f_d$  is a scaling factor ranging from 0 to 255,  $\rho_{\text{def}}$  is the default soil density from the material list,  $p$  is porosity,  $\theta_{\text{cod}}$  is the VWC associated with the selected material type, and  $\rho_w$  is the density of water, assumed to be 1, g/cm<sup>3</sup>.

A key objective of the simulations was to evaluate the system's response under heterogeneous soil conditions. For this purpose, numerous simulations were conducted by systematically varying the soil porosity to emulate density changes. Notably, reducing density by replacing soil with void (rather than adjusting water content) has a comparatively minor effect on neutron moderation, which remains predominantly governed by the presence of hydrogen even for small VWC content. Therefore, this strategy does not significantly compromise the validity of the results.

### 3.3.3 Footprint estimation

Given the computational cost associated with neutron simulations, the initial set of experiments focused on a qualitative assessment of the neutron footprint. This step was crucial to determine an optimal source design: a source that is too small may yield unrepresentative results, whereas an excessively large source increases computational burden without added benefit.

All simulations were executed on a university server equipped with 48 CPUs. Since URANOS runs each simulation on a single core, a standard of  $10^7$  neutrons per simulation was adopted, balancing statistical robustness and computation time (typically 1–2 hours). Simulations requiring higher precision were conducted by running multiple instances in parallel under identical conditions and aggregating the neutron

counts for subsequent analysis.

The simulation geometry remained consistent throughout: the neutron source was defined between 80 and 30, m above ground level (agl), the detector layer spanned from 2.5 to 1.5, m agl, and the soil layer extended to 3, m below ground level (bgl). A virtual detector, a 3, m diameter circular probe placed at the center of the domain, was preferred over an infinite detection layer, as it offers a more realistic representation while retaining computational efficiency. This choice reflects a compromise, as real-world CRNS sensors typically have a diameter of less than 30, cm.

To understand the footprint behavior and guide source dimensioning, approximately 20 simulations were performed with varying source sizes and domain extents. Results revealed that the source field in URANOS features a central plateau where intensity remains relatively constant, surrounded by a transition zone with decreasing intensity (Figure 3.14). As a result, it is advisable for the source radius to exceed the domain of interest by at least 200, m to avoid edge effects.

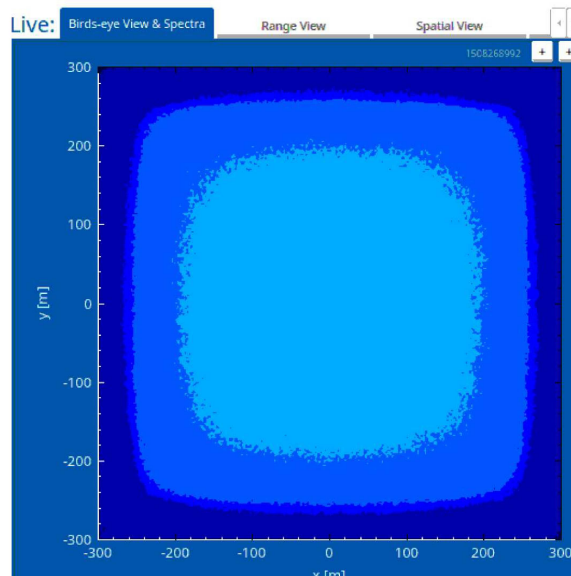


Figure 3.14: Source plateau example. With a source radius of 250, m, edge effects are visible, extending approximately 100, m inward from the boundary.

For example, targeting a domain of  $600 \times 600$ , m would require a source radius of at least 500, m to ensure consistent results across the region of interest.

Under the specific environmental conditions of Borgo Grignanello, summarized in

3.5, and two different density conditions, obtained by using different porosities (35% and 70%) the estimated neutron footprint ranged between 200 and 300 m, while the penetration depth, defined as the depth within which 86% of the detected neutrons experienced their first interaction with the ground, varied from approximately 15 to 65 cm with water content. Representative results for two soil types with different porosities are reported in Table 3.4.

These values were derived from the output of the URANOS simulations. Among other variables, the software records both the maximum depth reached by each detected neutron that interacted with the soil and the  $(x, y, z)$  coordinates of its first soil interaction. A simple post-processing code was developed to extract the footprint and penetration depth under consistent statistical conditions. Specifically, the footprint was calculated by progressively increasing the horizontal search radius in steps of 1 m until 86% of the detected neutrons were included, resulting in a maximum deviation of 0.5%. Similarly, the penetration depth was obtained by incrementally extending the vertical search depth in steps of 1 cm, achieving an uncertainty of 0.2% in the neutron population considered.

VWC [%]	35% porosity		70% porosity	
	Footprint [m]	$z_{86}$ [cm]	Footprint [m]	$z_{86}$ [cm]
3	281	38.6	269	63.7
7	286	27.6	308	43.3
10	293	27.1	274	36.2
15	263	23.3	278	31.6
20	234	19.5	206	26.7
30	252	16.3	271	20.3

Table 3.4: Neutron footprint and depth ( $z_{86}$ ) for simulations with  $5 \cdot 10^7$  neutrons under two different porosity scenarios.

### 3.3.4 Count - VWC curves

Once a reliable simulation protocol was established, it became possible to explore neutron propagation and its interaction with varying soil moisture conditions. To this end, a series of simulations were conducted to reproduce the expected hyperbolic relationship between neutron count and volumetric water content (VWC). A total of

12 simulations were performed, covering a range of VWC values: [3, 7, 10, 15, 20, 30] %, under two distinct porosity conditions (see Table 3.4).

The first porosity value, 70%, was selected to reflect the soil conditions observed at the Borgo Grignanello site, where bulk densities typically range between 0.8 and 0.9, g/cm<sup>3</sup>. This choice can be justified using Equation 3.3:

$$\rho = ((1 - 0.7) \cdot 2.86 + \theta \cdot 1) \text{ g/cm}^3 \quad (3.4)$$

$$= (0.85 + \theta \cdot 1) \text{ g/cm}^3 \quad (3.5)$$

where 2.86, g/cm<sup>3</sup> corresponds to the default soil density in URANOS for 0% porosity. A second porosity level, 35%, was also tested for comparison, resulting in a higher bulk density of approximately 1.86, g/cm<sup>3</sup>.

The simulation setup, including geometry and environmental parameters, is summarized in Table 3.5. These values remained consistent across all simulations described in this and next sections.

source layer:	30 – 80 m agl
detector layer:	1.5 – 2.5 m agl
detector diameter:	3 m
ground layer:	0 – 3 m bgl
square source half-size:	500 m
air humidity:	16 g/m <sup>3</sup>
air hum. exp: l.	Inf
atmospheric depth:	1013g/cm <sup>2</sup>
cutoff rigidity:	5 GeV
input neutrons:	5 · 10 <sup>7</sup>

Table 3.5: Geometrical and physical parameters representative of the Borgo Grignanello site, shared by all simulations.

The resulting neutron counts are shown in Figure 3.15, normalized with respect to the count at the lowest VWC value in each group. In both porosity cases, the data fit very well ( $R^2 > 99\%$ ) with a hyperbola, which is consistent with eq. 2.4 .

A notable difference in absolute neutron count can be observed between the two soil types. The denser material (i.e., with lower porosity) consistently results in

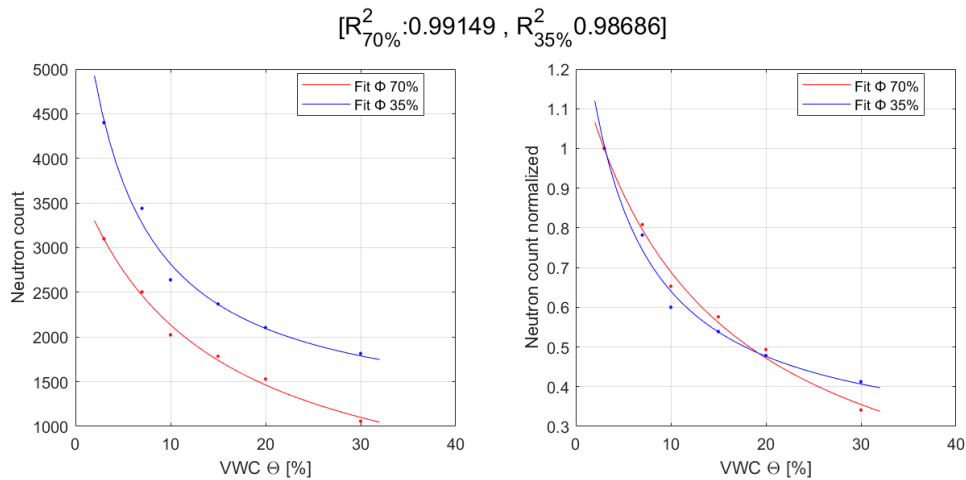


Figure 3.15: Neutron count (left) and normalized neutron count (right) as a function of VWC for two porosity conditions. The data exhibit a hyperbolic trend, as expected from theory. In the title the  $R^2$  of the fit are written

a higher count rate. This phenomenon can be attributed to the reduced mean free path in denser media, leading to more frequent interactions. Although these interactions are primarily elastic scattering with heavier compounds, which do not significantly reduce neutron energy, they contribute to greater backscattering toward the detector. Since atmospheric humidity is relatively low, neutrons that remain in the upper soil layers or atmosphere are less likely to be moderated, or to "get lost" in the deeper soil, thereby increasing the probability of detection.

Despite the limited number of simulations, some preliminary conclusions can be drawn. As shown in Table 3.4, the penetration depth ( $z_{86}$ ) for the higher-density material is approximately 20% to 40% shallower compared to the lower-density case. This observation further supports the interpretation that after VWC, the bulk density plays an important role in the neutron transport in the ground.

### 3.3.5 Assessing the effect of the field heterogeneity

This section investigates whether, under heterogeneous soil conditions, the response of a cosmic-ray neutron sensor (CRNS) is predominantly controlled by one specific region and, if so, which one. From a theoretical perspective, the non-linear relationship between neutron counts and volumetric water content (VWC) suggests that the driest region should dominate the signal. However, this must be considered along-

side the non trivial spatial sensitivity function of the detector (sec. 2.1.3), which plays a critical role whenever spatial heterogeneity is present. Understanding this behavior is essential for translating insights from simulations into the interpretation of field observations.

The approach consisted of running a series of heterogeneous simulations and comparing their neutron counts and converted VWC values with those from analogous homogeneous simulations that matched the properties of the individual regions. This comparison makes it possible to evaluate the relative contribution of each region to the overall neutron signal and to better characterize the system's behavior.

The definition of the heterogeneous regions was guided by geophysical data, in particular electromagnetic induction (EMI) inversion results, supported by geological interpretation (Figure 3.16). Two main units were identified: Region 1, on the western side of the site, predominantly fractured marl, and Region 2, on the eastern side, composed of silty loam.

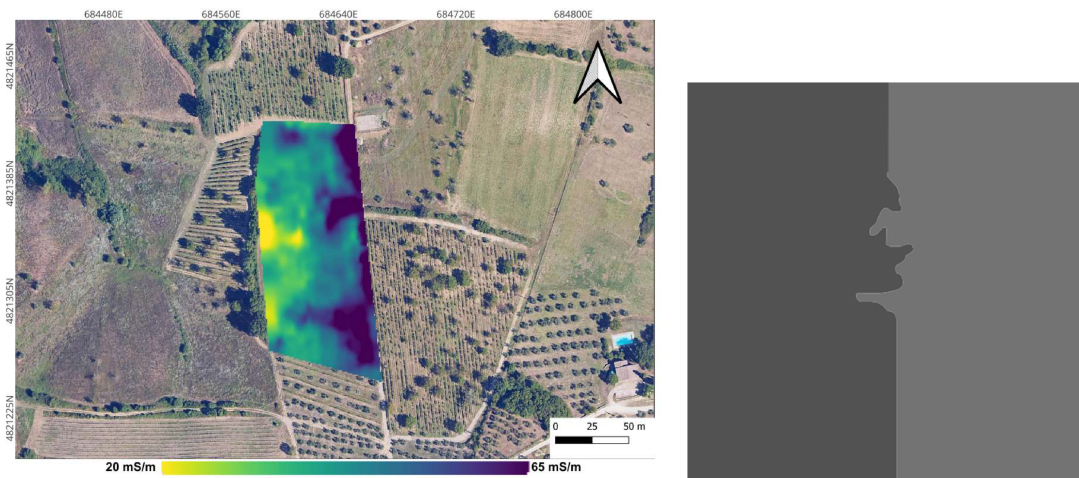


Figure 3.16: **Left:** EMI inversion map (1.25 m bgl), calibrated with a 40 cm-spacing 72-electrode ERT line and interpolated using kriging. **Right:** Example of grayscale PNG input used in URANOS to encode spatially variable porosity and soil water content. The map models the 500m  $\times$  500m field centred in the detector.

Four simulations were carried out to explore the neutron response under different moisture conditions in these two materials. VWC values were chosen to reflect realistic ranges and dynamics; in fact, we expect drier conditions and more rapid infiltration, evapotranspiration (ET), and root water uptake (RWU) dynamics in the fractured marl area (Region 1) rather than in the silty loam one (Region2). For this

reason, we chose VWC values of [5, 10, 15, 25]% for the first, and [30, 32.5, 35, 40]% for the second region. Porosities were set to 30% and 50%, respectively.

To evaluate the role of the uppermost soil layer, an additional set of simulations included a homogeneous 30 cm-thick topsoil with properties derived from field samples (density = 0.9 g/cm<sup>3</sup>, resulting in porosity = 70% and VWC = 20%). As previously discussed, sample analysis did not reveal systematic vertical or spatial patterns in bulk density or VWC, suggesting that this simplified configuration is a reasonable approximation.

Table 3.6 summarizes the heterogeneous simulation setups. Each configuration was also repeated with the additional top layer for comparison. Figure 3.17 might represent a useful guide through the several simulations mentioned.

Sim	VWC [%] region 1 - marl	VWC [%] region 2 - loam
Sim 1	5	30
Sim 2	10	32.5
Sim 3	15	35
Sim 4	25	40

Table 3.6: Heterogeneous simulation configurations. Porosity is set to 30% in Region 1 and 50% in Region 2. All simulations were also repeated with a 30 cm homogeneous top layer.

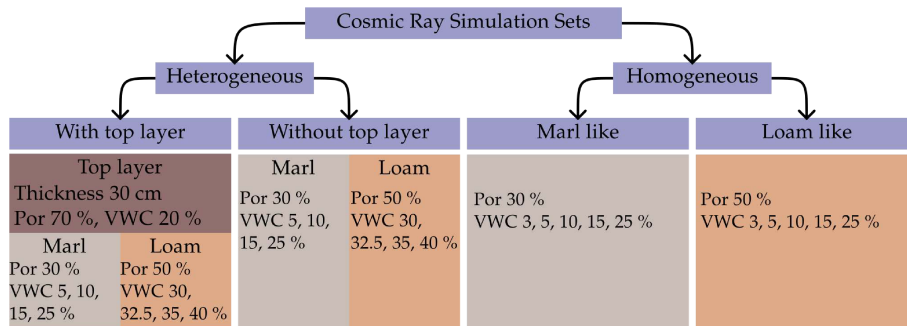


Figure 3.17: Figure summarizing, in an intuitive scheme, the several simulations performed for this section. On the right side, the homogeneous simulations were performed specifying the porosity used and the VWC investigated. On the left side, the specifics for the two regions, in one case covered with a superficial homogeneous layer.

The first investigations assess the role of the superficial homogeneous layer on the ground layer. Figure 3.18 presents the normalized count-VWC curves for both configurations, with and without the surface layer on the heterogenous ground.

Although no specific vertical patterns in moisture or density were observed in the

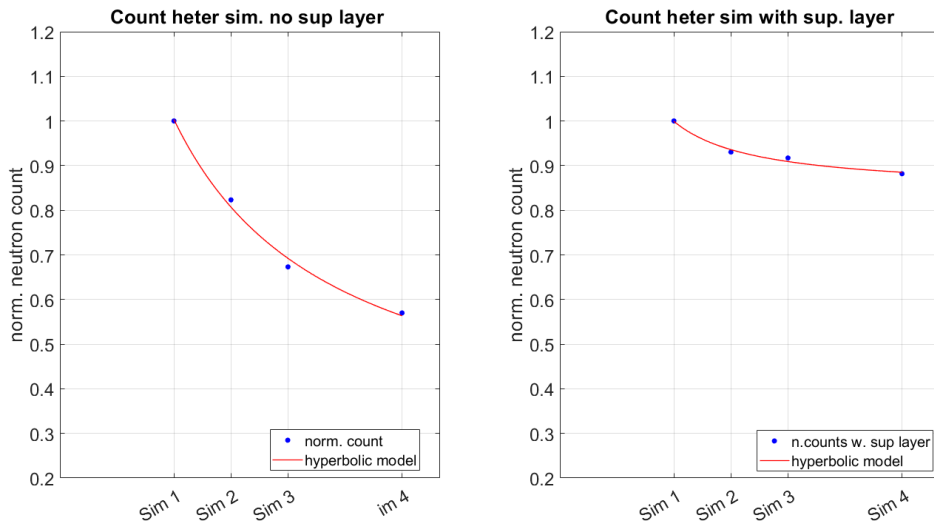


Figure 3.18: Normalized count–VWC curves for simulations with and without a 30 cm homogeneous top layer. Counts are plotted against the mean VWC of the two regions.

sample data, treating the upper soil layer as completely independent from the underlying material would oversimplify the hydrological system. Based on general principles of subsurface flow, it is reasonable to expect that lithological heterogeneities at depth also influence the behavior of the upper layer. For this reason, the simulations without the added superficial layer are considered more representative and are used in the analysis that follows.

The work hypothesis is that, in the presented geometrical configuration of the ground, the drier region dominates the neutron response. In other words, it should be possible to approximate the behavior of the heterogeneous site by that of a homogeneous site with the same characteristics as the dry region. The test for this consists of checking whether the VWC values derived from heterogeneous simulations align more closely with those of the marl unit than with those of the silty loam.

To establish this, homogeneous simulations were performed for both materials, using porosities of 30% and 50% and a common VWC range of 3, 5, 10, 15, 25 – %. As shown in Figure 3.19, the resulting curves confirm earlier observations: differences in porosity, i.e. bulk density, lead to differences in sensitivity of the neutron counts to changes in VWC and in the effective penetration depth.

The next step was to convert neutron counts into VWC. For this purpose, the

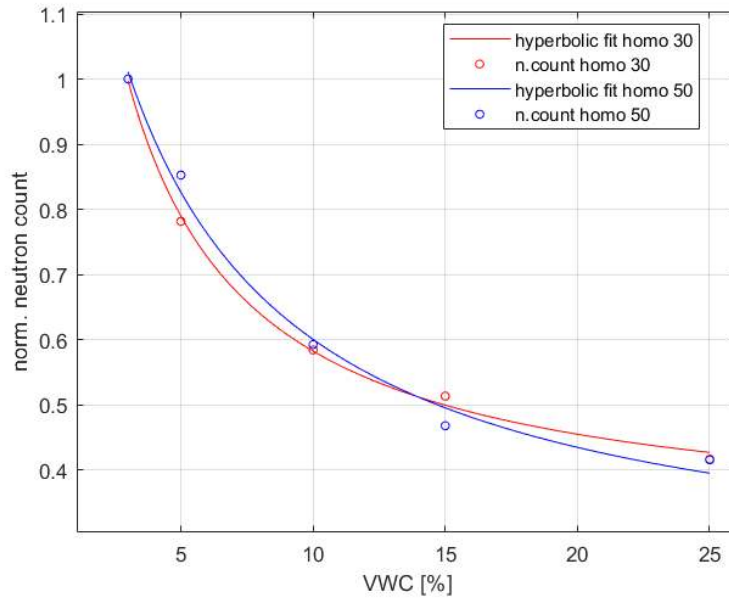


Figure 3.19: Normalized neutron counts for homogeneous configurations with 30% and 50% porosity.

software CoRNy<sup>3</sup> was used. CoRNy reads raw measurement files, performs basic quality control, applies correction functions, and provides a first-order soil water conversion. Its main input variable is the neutron count per second. However, synthetic counts strongly depend on the number of input neutrons and therefore on the computational power of the server used. As a consequence, they do not provide a realistic time–count relationship.

To overcome this, a scaling factor was introduced. A homogeneous simulation was run under site-specific conditions (bulk density, air pressure, and humidity) with  $5 \cdot 10^7$  input neutrons, consistent with all simulations in this work and 20% VWC. The resulting counts were compared with a field measurement on 17/04/2025 at 6 a.m., which, after conversion, yielded exactly 20% VWC. The scaling factor was then defined as:

$$N_{\text{cps}} = \frac{1400}{1875} \cdot \frac{N_{\text{synth}}}{3600} \quad (3.6)$$

where  $N_{\text{cps}}$  is the realistic neutron counts per second; 1400 is the measured neutron counts per hour corresponding to 20% VWC; and 1875 is the simulated neutron

<sup>3</sup>GitLab repository: [https://git.ufz.de/CRNS/cornish\\_pasdy](https://git.ufz.de/CRNS/cornish_pasdy)

counts for the same conditions.

The homogeneous simulations were also used to identify the most suitable CoRNy configuration, as several correction schemes are available. Since the synthetic setup already represented a simplified version of the field conditions, most of the corrections typically required for real data (e.g., organic matter, clay content, or variations in the incoming cosmic-ray flux) were not applied. Only air humidity and pressure corrections were included. Polynomial corrections were used for humidity, following [M. Köhli et al., 2021], as they provided the best results and are recommended for dry conditions. For air pressure, the exponential correction described by [Zreda et al., 2012] was adopted.

The conversion results for the homogeneous simulations are reported in Table 3.7. These values are particularly important as a test for assessing the robustness of the workflow. It should be noted, however, that each output originates from a single simulation, and thus some variability is expected due to statistical fluctuations. By contrast, real measurements are based on stacked data and moving averages over time windows, which naturally reduce variability. For this reason, deviations from the expected VWC output values are acceptable here, although further studies are planned to refine the statistical consistency of the results.

Model input	3%	5%	10%	15%	25%
CoRNy Output Marl (por = 30%)	1.19%	3.84%	9.42%	13.60%	25.07%
CoRNy Output Silty Loam (por = 50%)	1.74%	3.19%	9.39%	18.75%	27.33%

Table 3.7: Conversion results from CoRNy for homogeneous simulations corresponding to the two regions of the heterogeneous setup (Region 1, marl; Region 2, silty loam). The first row reports the VWC values used as input in the Monte Carlo ground model.

After establishing the best conversion settings (tested with Table 3.7 as results), counts from the heterogeneous simulations were also converted. Bulk density is a required input parameter for CoRNy; therefore, the process was carried out twice, once using  $\rho_b = 2.002 \text{ g/cm}^3$  (marl) and once using  $\rho_b = 1.43 \text{ g/cm}^3$  (silty loam). The results are presented in Table 3.8 and Figure 3.20.

To facilitate interpretation, the results of Table 3.8 are plotted together with the

Model input	5%–30%	10%–32.5%	15%–35%	25%–40%
CoRNy heter. site (1.43 g/cm <sup>3</sup> )	4.86%	8.50%	15.17%	25.34%
CoRNy heter. site (2.00 g/cm <sup>3</sup> )	6.80%	11.9%	21.24%	35.5%

Table 3.8: Conversion results from CoRNy for heterogeneous simulations. The first row reports the VWC inputs assigned to the ground model (Region 1 – Region 2).

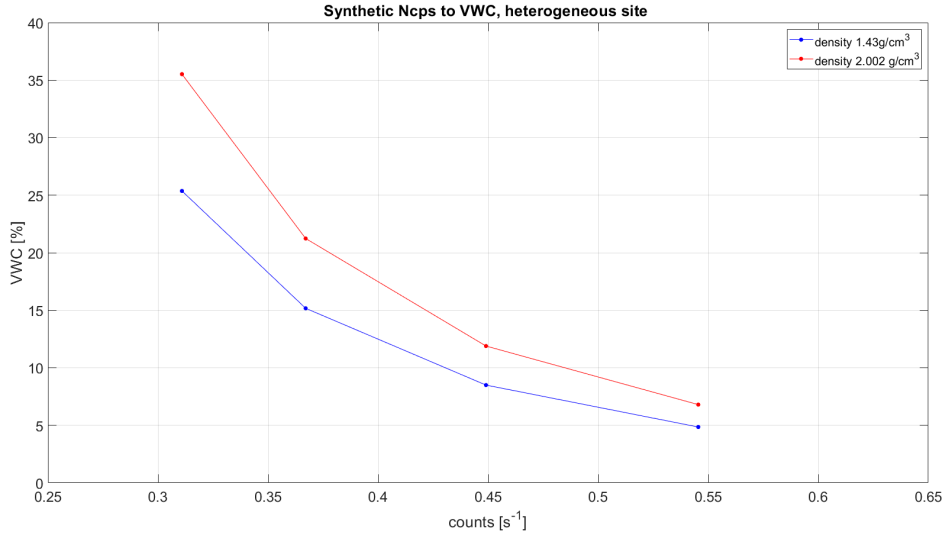


Figure 3.20: Results of the conversion with CoRNy for heterogeneous simulations. The two curves correspond to the conversions performed using the bulk densities of the two regions.

input values of VWC of the two regions in Figure 3.21.

At first glance, the last simulation appears to retrieve a VWC closer to that of the silty loam region. However, it must be emphasized that at higher water contents the conversion tends to overestimate VWC. This bias is likely linked to the air humidity correction, which is known to perform best under dry conditions. To test this, an additional set of homogeneous simulations was performed with silty loam at high water contents [30, 32.5, 35, 40]%. The results (Figure 3.22) confirmed that, when comparing converted values rather than input model values, the CRNS signal still aligns more closely with the drier region. The error associated with humidity correction thus appears to increase with VWC, leading to systematic overestimation in wetter soils. Nonetheless, the robustness of the workflow for the 0–25% VWC range is evident from Table 3.7, and within this range the dominance of the drier region is clearly demonstrated. This result supports the theoretical expectation that, under heterogeneous conditions, the CRNS response is disproportionately governed

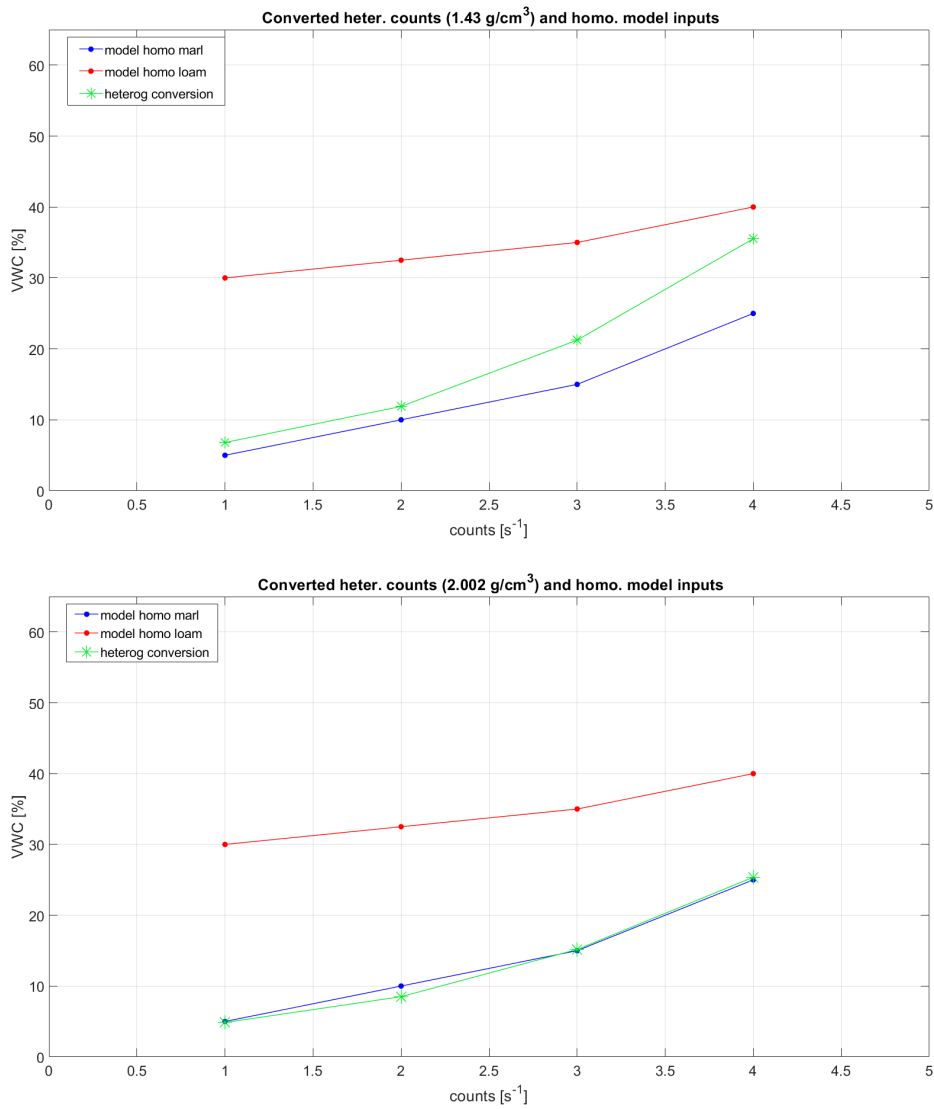


Figure 3.21: Heterogeneous simulation conversion results compared with the model input values of the two regions. The upper panel shows the results of the conversion performed using the silty loam bulk density for the whole field  $\rho_b = 1.43 \text{ g/cm}^3$ , whereas the lower panel with  $\rho_b = 2.002 \text{ g/cm}^3$ .

by the region with lower moisture content.

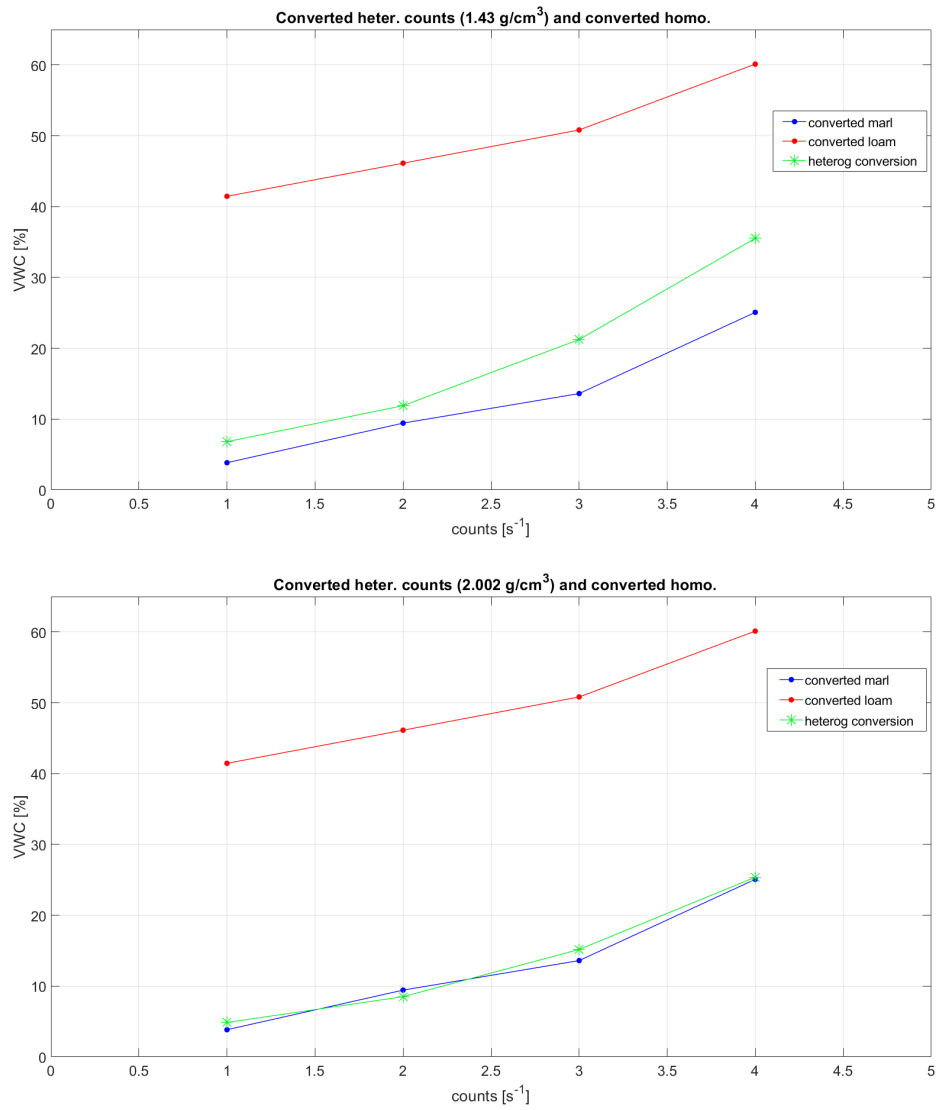


Figure 3.22: Heterogeneous conversion results (as in Fig. 3.21) plotted together with the conversion results of the homogeneous cases. Upper panel:  $\rho_b = 1.43 \text{ g/cm}^3$ ; lower panel:  $\rho_b = 2.002 \text{ g/cm}^3$ .



# Chapter 4

## Results and Discussion

### 4.1 Results from the Samples, ERT and EM

The EMI survey (Figure 3.10) confirmed the presence of two main lithologies at the site. The survey provided a rapid characterization of the shallow subsurface and proved useful for defining the locations of the ERT lines in a data-driven manner. Even before calibration with ERT data, the EMI inversion reproduced earlier observations of a very well-defined separation between the regions, thus giving confidence in the robustness of the survey.

Following this, a series of ERT lines were acquired to complement the EMI results. The aim was twofold: to enhance resolution at greater depths and to obtain a more accurate image of the subsurface structures. The ERT results revealed a conductive body overlying and intruding as a lens into a more resistive formation. Geological information from the site, combined with observations of nearby outcrops, suggests that the resistive unit corresponds to a marly lithology. This interpretation is consistent with the resistivity values obtained from the surveys, which fall in the range of  $\approx 40 \Omega\text{m}$  to  $60 \Omega\text{m}$  and are compatible with fractured marl in the shallow subsurface. The conductive region, by contrast, exhibited resistivities of  $\leq 10 \Omega\text{m}$ , indicative of higher porosity materials and possibly enriched in clay.

The ERT data further indicate that the silty loam lens reaches several meters in thickness. This is significantly greater than the penetration depth of the CRNS method and therefore supports the use of a uniform model in depth for the simu-

lations. Importantly, the combined EMI–ERT dataset confirms earlier site characterizations and demonstrates the presence of substantial lateral heterogeneity that extends beyond the vineyard where most measurements were carried out.

Additional constraints were obtained from the laboratory analysis of soil samples. These confirmed a high proportion of silty loam and revealed a significant organic matter content of approximately 9% in the upper 25 cm across different sampling locations. No systematic spatial trend or depth gradient was observed in bulk density or VWC, suggesting that the very first soil layer can be considered homogeneous at the scale of interest. In conclusion, the measurements confirmed earlier findings while providing higher-resolution images of the subsurface. This enabled a more detailed comparison between geophysical proxies for hydrological parameters and CRNP data over the relevant periods.

## 4.2 Results from the simulations and analysis

The simulation campaign was designed to serve three purposes: first, to deepen the understanding of the physical principles underlying CRNS; second, to develop practical skills in simulating neutron propagation and interactions using URANOS, a state-of-the-art tool for environmental neutron physics; and third, to extend the interpretation of CRNS data by integrating insights from complementary geophysical methods.

The footprint study provided valuable methodological insights into the use of URANOS, while also delivering results consistent with those in the literature. In particular, the simulations confirmed that the effective detector footprint radius is on the order of 250 m – 300 m in ideal conditions such synthetic setups.

The analysis of porosity effects demonstrated that variations in soil density do not play the main role in when studying the count dynamics, in fact the VWC dominates. However, interesting features might be noticed when the VWC is not high; in fact, the results show that with lower bulk density both the footprint and penetration depth (Figure 3.4) increase, while the overall count decreases. This effect tends to disappear with increasing moisture. These preliminary findings provided the basis

for designing more complex simulations of heterogeneous soil models.

The heterogeneous simulations, discussed in detail in Section 3.3, yielded promising results directly aligned with the central hypothesis of this thesis. The comparison between heterogeneous and homogeneous setups demonstrated that the neutron response of a heterogeneous site can, to a good approximation, be represented by that of a homogeneous model with properties matching those of the drier region. After conversion of neutron counts into VWC, the agreement between heterogeneous and homogeneous results was particularly close when the density assumed for the conversion matched that of the drier material.

These findings demonstrate that, during both drying and wetting phases, the CRNS signal is predominantly governed by the driest region. Accordingly, within certain VWC ranges, the dynamics of a heterogeneous system may be reasonably approximated by those of a homogeneous model characterized by the properties (e.g., porosity and VWC) of the driest lithology. This behavior is consistent with theoretical expectations, since regions with lower water content moderate neutrons less effectively and therefore contribute disproportionately to the detected signal. The simulations provide quantitative confirmation of this effect.

From an applied perspective, the results suggest that when prior information about subsurface heterogeneity is available, for instance from EMI or ERT surveys, CRNS data can be interpreted with greater confidence by referencing the dominant region. In this way, neutron count variations can be more reliably attributed to specific subdomains within the footprint. This significantly enhances the interpretability of CRNS measurements and increases their value for field-scale soil moisture monitoring.

Nevertheless, it is important to recall the detector's non-trivial radial weighting (sensitivity) function (see Sec. 2.1.3). Consequently, the conclusion presented is geometry-dependent: for heterogeneity patterns that differ markedly from the two-region configuration implemented here, the analysis should be replicated with the appropriate site-specific geometry to assess the impact of the spatial arrangement on the CRNS response.



# Conclusions

The purpose of this work originates from the need to bridge the gap between the large-scale soil moisture information provided by remote sensing and the highly local information obtained from point sensors, which remain the state of the art for soil water content monitoring. Such intermediate-scale information is increasingly demanded in applied contexts, from agricultural resource management to the assessment of slope stability and landslide hazard.

In this thesis, the interpretation of CRNS data was supported by a study of the theoretical background of cosmic ray particles, with particular attention to neutron interactions and detection principles. Beyond the literature review, extensive numerical simulations were carried out using the URANOS software. These allowed to explore different environmental conditions and test the influence of several key variables. The simulations confirmed and extended existing knowledge of the CRNS penetration depth and footprint, estimated here between  $\sim 200$  and  $\sim 300$  m in radius and 15–65 cm in depth, respectively. Furthermore, the expected semi-empirical hyperbolic relation between neutron counts and volumetric water content (VWC) was successfully reproduced under simplified conditions. As expected, the agreement was strongest in the “ideal world” of simulations, where environmental complexity is absent and where more advanced models, such as the UTS approach, are not required.

The role of soil density was also investigated. Synthetic data showed that density exerts a stronger influence at low VWC values, with its main effect lying in changes to the probe footprint and penetration depth. Denser materials do not moderate neutrons more efficiently, but they reduce the mean free path, thereby enhancing scattering back toward the detector, reducing both the quantities in depth and

distance.

The study then turned to the case of heterogeneous sites. Since CRNS provides integrated measurements over its footprint, it lacks spatial resolution. However, because of the non-trivial spatial weighting function of the detector and the non-linear count–VWC relationship, it was hypothesized that, for the specific geometry at Borgo Grignanello, the region with lower VWC would dominate the signal. In practical terms, this means that the drying and wetting dynamics of the heterogeneous site could be approximated by the response of a homogeneous system defined by the properties of the drier lithology. This line of reasoning also responds to the need to provide decision-makers with straightforward interpretative schemes, without compromising scientific rigor.

The results of the simulations support this hypothesis. Comparisons between heterogeneous two-region simulations and homogeneous counterparts showed that, at low VWC, the converted values from the heterogeneous setup closely matched those of the drier (marl) region. The approximation was robust within the investigated ranges. It must be stressed, however, that because of the complex radial weighting function of the detector, these results cannot be generalized to arbitrary heterogeneity patterns. The geometry studied here, characterized by an almost symmetric two-region configuration relative to the detector, is a specific case that requires further testing under different spatial arrangements.

Despite this caveat, the findings are promising and highlight the potential of CRNS for practical applications. The methodology presented is scientifically meaningful, though additional rigor is required to strengthen the robustness of the results. In particular, future work should include a more statistically consistent exploration of heterogeneous conditions. This would require performing multiple simulation runs for each VWC scenario to provide a more reliable conversion into VWC using the CoRNy tool. Moreover, while the main objective of this thesis has been achieved, further effort should be devoted to improving the conversion of synthetic counts for the silty loam region (higher VWC values), where the values obtained were less consistent than expected. Ultimately, the results presented here contribute to the broader effort of positioning CRNS as a robust intermediate-scale monitoring tech-

---

nique within the critical zone, capable of complementing both remote sensing and traditional point-scale approaches for the study of soil–plant–atmosphere interactions.

## CONCLUSIONS

---

# Bibliography

- Binley, A., Hubbard, S. S., Huisman, J. A., Revil, A., Robinson, D. A., Singha, K., & Slater, L. D. (2015). The emergence of hydrogeophysics for improved understanding of subsurface processes over multiple scales. *Water resources research*, *51*(6), 3837–3866.
- Blanchy, G., Saneiyani, S., Boyd, J., McLachlan, P., & Binley, A. (2020). Resipy, an intuitive open source software for complex geoelectrical inversion/modeling. *Computers & Geosciences*, *137*, 104423. <https://doi.org/10.1016/j.cageo.2020.104423>
- Camporese, M., Cassiani, G., Deiana, R., Salandin, P., & Binley, A. (2015). Coupled and uncoupled hydrogeophysical inversions using ensemble kalman filter assimilation of ert-monitored tracer test data. *Water Resources Research*, *51*(5), 3277–3291.
- Cassiani, G., Boaga, J., Rossi, M., Putti, M., Fadda, G., Majone, B., & Bellin, A. (2016). Soil–plant interaction monitoring: Small scale example of an apple orchard in trentino, north-eastern italy. *Science of the Total Environment*, *543*, 851–861.
- Cassiani, G., Boaga, J., Vanella, D., Perri, M. T., & Consoli, S. (2015). Monitoring and modelling of soil–plant interactions: The joint use of ert, sap flow and eddy covariance data to characterize the volume of an orange tree root zone. *Hydrology and Earth System Sciences*, *19*(5), 2213–2225.
- Clem, J. M., & Dorman, L. I. (2000). Neutron monitor response functions. *Cosmic Rays and Earth: Proceedings of an ISSI Workshop, 21–26 March 1999, Bern, Switzerland*, 335–359.

- Constable, S. C., Parker, R. L., & Constable, C. G. (1987). Occam's inversion: A practical algorithm for generating smooth models from electromagnetic sounding data. *Geophysics*, *52*(3), 289–300.
- Desilets, D., & Zreda, M. (2013). Footprint diameter for a cosmic-ray soil moisture probe: Theory and monte carlo simulations. *Water Resources Research*, *49*(6), 3566–3575.
- Desilets, D., Zreda, M., & Ferré, T. P. (2010). Nature's neutron probe: Land surface hydrology at an elusive scale with cosmic rays. *Water Resources Research*, *46*(11).
- Forget, P., et al. (2010). Neutron interactions and applications.
- Gaisser, T. K. (2006). The cosmic-ray spectrum: From the knee to the ankle. *Journal of Physics: Conference Series*, *47*(1), 15. <https://doi.org/10.1088/1742-6596/47/1/002>
- Goldhagen, P. (2003). Cosmic-ray neutrons on the ground and in the atmosphere. *MRS bulletin*, *28*(2), 131–135.
- Horvath, H. (1988). Experimental investigation on the validity of the lambert-beer law at high particle concentrations [Sixteenth Annual Conference of the Gesellschaft fur Aerosolforschung]. *Journal of Aerosol Science*, *19*(7), 837–840. [https://doi.org/https://doi.org/10.1016/0021-8502\(88\)90046-8](https://doi.org/https://doi.org/10.1016/0021-8502(88)90046-8)
- Köhli, M., Schrön, M., & Schmidt, U. (2018). Response functions for detectors in cosmic ray neutron sensing. *Nuclear instruments and methods in physics research section A: Accelerators, spectrometers, detectors and associated equipment*, *902*, 184–189.
- Köhli, M., Schrön, M., Zreda, M., Schmidt, U., Dietrich, P., & Zacharias, S. (2015). Footprint characteristics revised for field-scale soil moisture monitoring with cosmic-ray neutrons. *Water Resources Research*, *51*(7), 5772–5790.
- Köhli, M., Weimar, J., Schrön, M., Baatz, R., & Schmidt, U. (2021). Soil moisture and air humidity dependence of the above-ground cosmic-ray neutron intensity. *Frontiers in Water*, *2*, 544847.
- Köhli, M. O. (2019). The cascade 10 b thermal neutron detector and soil moisture sensing by cosmic-ray neutrons.

- Masnaghetti, A. (2022). Uga additional geographic unit. *ENOGEA Alessandro Masnaghetti Editore*. [https://eadn-wc02-8007516.nxedge.io/wp-content/uploads/2023/05/Terreno-Chianti-Classico-Geography.pdf?utm\\_source=chatgpt.com](https://eadn-wc02-8007516.nxedge.io/wp-content/uploads/2023/05/Terreno-Chianti-Classico-Geography.pdf?utm_source=chatgpt.com)
- McLachlan, P., Blanchy, G., & Binley, A. (2021). Emagpy: Open-source standalone software for processing, forward modeling and inversion of electromagnetic induction data. *Computers & Geosciences*, *146*, 104561. <https://doi.org/https://doi.org/10.1016/j.cageo.2020.104561>
- McNeeill, J. (1980). Electromagnetic terrain conductivity measurement at low induction numbers. *Geonics technical note TN-6*.
- Paul, S. (2009). The puzzle of neutron lifetime [Particle Physics with Slow Neutrons]. *Nuclear Instruments and Methods in Physics Research Section A: Accelerators, Spectrometers, Detectors and Associated Equipment*, *611*(2), 157–166. <https://doi.org/https://doi.org/10.1016/j.nima.2009.07.095>
- Regione-Toscana. (2007). Legenda unità geologiche e depositi superficiali. [https://www502.regione.toscana.it/geoscopio/hotlinks/geologia/banca\\_dati\\_geologica/legenda/Legenda\\_unita\\_geologiche\\_e\\_depositi.pdf?utm\\_source=chatgpt.com](https://www502.regione.toscana.it/geoscopio/hotlinks/geologia/banca_dati_geologica/legenda/Legenda_unita_geologiche_e_depositi.pdf?utm_source=chatgpt.com)
- Sato, T., & Niita, K. (2006). Analytical functions to predict cosmic-ray neutron spectra in the atmosphere. *Radiation research*, *166*(3), 544–555.
- Schrön, M., Köhli, M., Scheiffle, L., Iwema, J., Bogena, H. R., Lv, L., Martini, E., Baroni, G., Rosolem, R., Weimar, J., et al. (2017). Improving calibration and validation of cosmic-ray neutron sensors in the light of spatial sensitivity. *Hydrology and Earth System Sciences*, *21*(10), 5009–5030.
- Schrön, M., Rosolem, R., Köhli, M., Piussi, L., Schröter, I., Iwema, J., Kögler, S., Oswald, S., Wollschläger, U., Samaniego, L., et al. (2018). Cosmic-ray neutron rover surveys of field soil moisture and the influence of roads. *Water Resources Research*, *54*(9), 6441–6459.
- Sears, V. F. (1992). Neutron scattering lengths and cross sections. *Neutron news*, *3*(3), 26–37.

- Köhli, M., & Weimar, J. O. (2024). *Stx s2+ cosmic ray neutron detector, technical reference manual*. StyX Neutronica GmbH.
- Uhlemann, S., Peruzzo, L., Chou, C., Williams, K., Wielandt, S., Wang, C., Falco, N., Wu, Y., Carr, B., Meldrum, P., et al. (2024). Variations in bedrock and vegetation cover modulate subsurface water flow dynamics of a mountainous hillslope. *Water Resources Research*, *60*(2), e2023WR036137.
- Vanderborght, J., Huisman, J., Van der Kruk, J., & Vereecken, H. (2013). Geophysical methods for field-scale imaging of root zone properties and processes. *Soil–water–root processes: advances in tomography and imaging*, *61*, 247–282.
- Wang, X., Liu, R., Köhli, M., Marach, J., & Wang, Z. (2025). Monitoring soil water content and measurement depth of cosmic-ray neutron sensing in the tibetan plateau. *Journal of Hydrometeorology*, *26*(2), 155–167.
- Weimar, J. O. (2022). *Advances in cosmic-ray neutron sensing by monte carlo simulations and neutron detector development* [Doctoral dissertation].
- Ziegler, J. F. (1996). Terrestrial cosmic rays. *IBM journal of research and development*, *40*(1), 19–39.
- Zreda, M., Desilets, D., Ferré, T., & Scott, R. L. (2008). Measuring soil moisture content non-invasively at intermediate spatial scale using cosmic-ray neutrons. *Geophysical research letters*, *35*(21).
- Zreda, M., Shuttleworth, W., Zeng, X., Zweck, C., Desilets, D., Franz, T., & Rosolem, R. (2012). Cosmos: The cosmic-ray soil moisture observing system. *Hydrology and Earth System Sciences*, *16*(11), 4079–4099.

# Acknowledgments

This work has been made possible thanks to the invaluable support of the Geophysics group within the Department of Geosciences, both in terms of scientific guidance and human presence. I am deeply grateful to my supervisors: Dr. Luca Peruzzo, with whom I had the privilege to work in close synergy throughout this project, and who guided me through the research and development of the entire work; and Professor Giorgio Cassiani, whom I regard as a true mentor. His guidance, along with the intellectual vision and reasoning he imparted to me, not only inspired me throughout these two years, but will continue to shape my personal and professional development.

This work would not have been possible without the generous support of Markus Köhli and Jannis Weimar (University of Heidelberg), who guided us with remarkable availability and enthusiasm, from understanding the theoretical concepts to the instrumentation setup and software implementation.

I also wish to express my sincere thanks to Mirko Pavoni, Matteo Censini, and Francesca Manca, whose contributions in the field have been invaluable.

Beyond the research itself, this work represents a chapter of my life's journey, shaped by growth, challenges, and many memorable experiences. Along this path, I have been fortunate to share moments, support, and inspiration with remarkable friends; therefore, my heartfelt gratitude goes to Lala, Ivan, Alessandro, and Federica, as also I am especially grateful to Sofia, who has been by my side from the very beginning and continues to be. Finally, I owe my deepest thanks to my family and to Alex, who, despite all difficulties, have always remained supportive and resilient, and of whom I am profoundly proud. I would like to dedicate to the following lines.

*We never know how high we are  
Till we are called to rise;  
And then, if we are true to plan,  
Our statures touch the skies.*

...

*Emily Dickinson*